JGR Solid Earth

RESEARCH ARTICLE
10.1029/2022JB026070

How Do Earthquakes Stop? Insights From a Minimal Model of Frictional Rupture

Fabian Barras[1], Kjetil Thøgersen[1], Einat Aharonov[1,2], and François Renard[1,3]

[1]Departments of Geosciences and Physics, The Njord Centre, University of Oslo, Oslo, Norway, [2]Institute of Earth Sciences, The Hebrew University, Jerusalem, Israel, [3]ISTerre, Univ. Grenoble Alpes, Grenoble INP, Univ. Savoie Mont Blanc, CNRS, IRD, Univ. Gustave Eiffel, Grenoble, France

Key Points:

- A minimal model of frictional rupture describes large earthquake ruptures
- Two parameters, the dimensionless pre-stress and fracture energy, account for previously proposed mechanisms of earthquake arrest
- The model illuminates the different energy balance that drives crack-like and pulse-like ruptures and control the asymmetry of slip profiles

Supporting Information:

Supporting Information may be found in the online version of this article.

Correspondence to:

F. Barras,
fabian.barras@mn.uio.no

Citation:

Barras, F., Thøgersen, K., Aharonov, E., & Renard, F. (2023). How do earthquakes stop? Insights from a minimal model of frictional rupture. *Journal of Geophysical Research: Solid Earth*, *128*, e2022JB026070. https://doi.org/10.1029/2022JB026070

Received 17 NOV 2022
Accepted 20 JUN 2023

Author Contributions:

Conceptualization: Fabian Barras, Kjetil Thøgersen, Einat Aharonov, François Renard
Funding acquisition: François Renard
Investigation: Fabian Barras, Kjetil Thøgersen, Einat Aharonov, François Renard
Software: Fabian Barras, Kjetil Thøgersen
Writing – original draft: Fabian Barras, Kjetil Thøgersen, Einat Aharonov, François Renard
Writing – review & editing: Fabian Barras, Kjetil Thøgersen, Einat Aharonov, François Renard

Abstract The question "what arrests an earthquake rupture?" sits at the heart of any potential prediction of earthquake magnitude. Here, we use a one-dimensional, thin-elastic-strip, minimal model, to illuminate the basic physical parameters that may control the arrest of large ruptures. The generic formulation of the model allows for wrapping various earthquake arrest scenarios into the variations of two dimensionless variables $\bar{\tau}_k$ (initial dimensionless stress parameter on the fault) and $\bar{G}_c$ (dimensionless fracture energy), valid for both in-plane and antiplane shear loading. Our continuum model is equivalent to the standard Burridge-Knopoff model, with an added characteristic length scale, H, that corresponds to either the thickness of the damage zone for strike-slip faults or to the thickness of the downward moving plate for subduction settings. We simulate the propagation and arrest of frictional ruptures and derive closed-form expressions to predict rupture arrest under different conditions. Our generic model illuminates the different energy budget that mediates crack- and pulse-like rupture propagation and arrest. It provides additional predictions such as generic stable pulse-like rupture solutions, stress drop independence of the rupture size, the existence of back-propagating fronts, and predicts that asymmetric slip profiles arise under certain pre-stress conditions. These diverse features occur also in natural earthquakes, and the fact that they can all be predicted by a single minimal framework is encouraging and pave the way for future developments of this model.

Plain Language Summary Untangling the dynamics that governs the propagation and arrest of earthquakes is still challenging, mainly because of the few constraints available on the fault zone geometry, the constitutive properties of fault materials, as well as fault rheology during the rupture event. The present study aims at formulating a model containing a minimal number of parameters to describe the dynamics of large earthquakes. Despite its simplicity, this minimal model is able to reproduce several salient features of natural earthquakes that are still debated (e.g., various arrest scenarios, stable pulse-like rupture, back-propagating front, asymmetric slip profiles). We demonstrate how the proposed model can be used to simulate the propagation and arrest of large earthquakes, which are controlled by local variations of shear stress and material properties on the fault. With this simple and generic description, the proposed model could be readily extended to account for additional processes controlling the dynamics of large earthquakes.

1. Introduction

Frictional rupture, the process by which a dynamic rupture propagates along a preexisting interface, has been proposed to control many geological processes, including earthquakes, landslides, glacier instabilities, and snow avalanches (e.g., Agliardi et al., 2020; Gabriel et al., 2012; Palmer and Rice, 1973; Scholz, 1998; Scholz, 2019; Thøgersen, Gilbert, et al., 2019; Trottet et al., 2022; Viesca and Rice, 2012; Weng and Ampuero, 2019). In these systems, a rupture nucleates at a given location along an interface, accelerates to a maximum velocity, and then decelerates until final arrest. The entire process is controlled by heterogeneities of the initial (normal and shear) stress conditions, geometry of the fault, and material properties along the interface and in the surrounding volume.

During frictional rupture, initial elastic strain energy stored in the volume around the interface is transformed into several components that involve (e.g., Cocco et al., 2023) (a) a transfer of elastic strain energy between different locations along the interface and in the volume around it (i.e., elastic stress redistribution); (b) near-fault dissipation accounting for co-seismic fracture and damage of the rock as well as frictional dissipation and heat production during slip; (c) emission of elastic waves (i.e., seismicity).

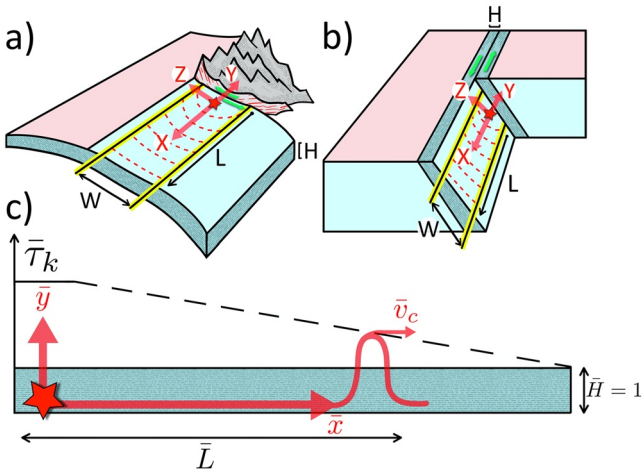

Figure 1. A minimal model to study frictional rupture arising along two types of plate boundaries, where loading is applied at a distance H from the fault. (a) Convergent (subduction zone or continental collision, H is the thickness of the down-moving plate), and (b) transform fault (strike-slip, H is the thickness of the damage zone). In panels (a) and (b), the direction of plate motion is shown by a pair of green arrows. Cross-sections reveal the frictional interface between the two tectonic plates as well as the seismogenic zone of width W that hosts dynamic ruptures. Earthquake propagation is depicted by the successive red dashed lines, starting from the nucleation location shown by the red stars, and L is the rupture length. Initially, the earthquake grows as a *circular crack* both along the strike and along the dip directions. As the size of the rupture exceeds H and W, the earthquake propagates as a *planar front* only along the strike direction. The profile of dimensionless stress parameter, $\bar{\tau}_k$, is sketched in panel (c) and has its peak in the nucleation zone set on the left of the domain. The propagation and arrest conditions are investigated in this study as the rupture propagates (rightwards) into a region less favorable to slip (lower pre-stress, higher frictional dissipation, geometrical barriers).

The arrest of frictional rupture can be predicted at the scale of laboratory experiments when rupture arises along the interface between two elastic blocks pressed in frictional contact (e.g., Bayart et al., 2016; Kammer et al., 2015; Ke et al., 2018). In this setup, the prediction builds upon the analogy to brittle shear fracture and requires to know an equivalent fracture energy of the frictional plane, which varies with the normal stress. Upscaling these predictions to natural earthquakes remains out of reach due to the complexity of the fault geometry (e.g., roughness, bends, segmentation), of the fault zone rheology (e.g., damage zone), as well as due to the difficulty in measuring stresses and how the various components of the earthquake energy budget interplay in transforming and consuming the initial elastic strain energy available before rupture propagation (e.g., Abercrombie and Rice, 2005; Barras et al., 2020; Brener and Bouchbinder, 2021; Cocco et al., 2023; Ke et al., 2022; Lambert and Lapusta, 2020; Paglialunga et al., 2021; Tinti et al., 2005). Prediction of rupture arrest is made even more difficult by the fact that earthquake propagation can arise under two distinct rupture modes; either crack-like or pulse-like (e.g., Lambert et al., 2021; Scholz, 2019). In conventional crack-like ruptures, also called circular cracks, all points within the growing ruptured area keep sliding until arrest (Burridge & Halliday, 1971; Kostrov & Das, 1988; Madariaga, 1976). Conversely, for pulse-like ruptures, a rupture front propagates along the interface and heals behind it, such that every point of the interface will accelerate, slip and arrest at different times (Heaton, 1990).

This complexity explains why a full comprehensive description of the conditions governing the arrest of an earthquake, and therefore its final size and magnitude, is still missing. Several scenarios of rupture arrest have been proposed in the literature and could be divided into two main categories. On the one hand, a rupture may stop because a local geometrical or mechanical heterogeneity, also called barrier, prevents further propagation (Aki, 1979; Das & Aki, 1977). On natural faults, a barrier could be related to fault segmentation (Harris & Day, 1999; Sibson, 1985; Sibson & Das, 1986; Wesnousky, 1988), to the fact that, near fault tip, rocks may be stronger and require more energy to break (e.g., concept of fault maturity, see Perrin et al. (2016)), or to variations in frictional properties (Marone & Scholz, 1988). On the other hand, a rupture may stop because of long-range variations of stress along the sliding interface. For example, if a fault has been unloaded by a previous earthquake, the shear stress along the interface will be lower than for a fault that has not broken for a long period and that has been loaded by tectonic stress during that period (e.g., Stein et al., 1997). In this situation, a frictional rupture may arrest because of the depletion of available elastic strain energy along a section of the fault. In other words, the rupture stops because it "runs out of steam."

Here, we explore the dynamics governing the propagation and arrest of frictional rupture by using a one-dimensional elastodynamic model that contains only two parameters in its dimensionless form (Thøgersen et al., 2021). A similar approach reproduces some observations made on slow, subshear, and supershear earthquakes, such as the scaling between duration and moment (Thøgersen, Sveinsson, et al., 2019). This minimal model builds on the approximation of the earthquake dynamics existing at the later stage of the rupture once its size exceeds the width of the seismogenic zone. The resulting one-dimensional formulation, summarized in Section 2, considers a thin elastic strip in frictional contact along a preexisting interface (Figure 1c), which may represent either a subduction setting (Figure 1a) or a strike-slip fault (Figure 1b) once the earthquake dynamics transition from *circular crack growth* toward the propagation of a *planar front*. Such transition is depicted by the successive dashed red lines in Figures 1a and 1b and have been reported in numerical simulations (Day, 1982; Weng & Ampuero, 2019), as well as from seismic inversion of natural earthquakes (Chen et al., 2020, 2022). The elastic strip is defined by its thickness, H, and two elastic parameters: the shear modulus $\mathcal{G}$ and the Lamé's first parameter λ, which can be related to the Poisson's ratio $\nu = 0.5\lambda(\lambda + \mathcal{G})^{-1}$. H may represent the plate thickness (Figure 1a) or the thickness of the damage zone (Figure 1b). More generally, this one-dimensional approximation applies to other kinds of frictional

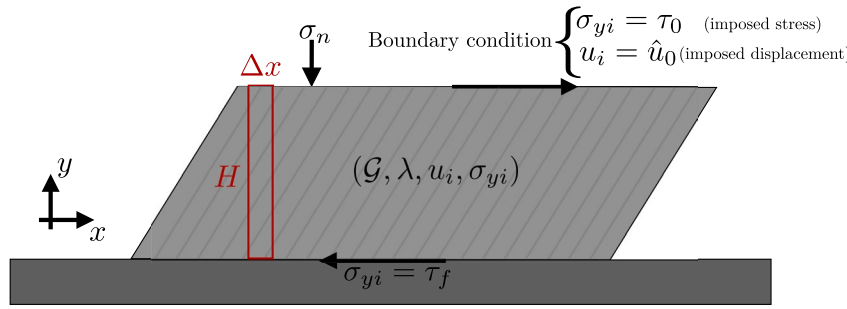

Figure 2. Sketch of the two-dimensional system that is integrated to obtain the one-dimensional equation of motion used in the manuscript. We model a thin elastic layer of thickness H with shear modulus $\mathcal{G}$ and the first Lamé coefficient λ. Two boundary conditions are considered on the top surface. At $y = H$ we apply either an imposed stress τ_0 or an imposed displacement $\hat{u}_0$. At $y = 0$, we apply a friction law. The system is integrated across the y-coordinate (red rectangle) to obtain a one-dimensional approximation. Modified from Thøgersen et al. (2021).

systems in which the rupture propagates as a planar front with length much larger than the off-plane thickness H (e.g., large normal-faulting earthquakes (Middleton et al., 2016), landslides (Germanovich et al., 2016), snow slab avalanches (Trottet et al., 2022)).

The model includes inertial effects in the direction of rupture propagation but neglects them in the normal direction. Along the interface, sliding occurs according to a friction law that either considers a sharp drop from static to dynamic friction (Amontons-Coulomb model) or accounts for a weakening distance and associated fracture energy (slip-weakening model). Rupture arrest is studied and discussed for these two friction models and two different rupture modes, crack versus pulse. Our approach is both numerical (Section 3) and analytical, since the simplicity of our model allows for the reproduction of a wide range of rupture arrest scenarios and their description with analytical expressions (Section 4). Using our minimal model, we present the boundary conditions that control the selection of the rupture mode (either pulse-like or crack-like) and describe the substantial difference that exists between these two modes in terms of the rupture energy balance and arrest conditions. The study concludes by highlighting how our one-dimensional framework bridges different earthquake models proposed in the literature and by discussing its implications for earthquake arrest in natural fault zones (Section 5).

2. A One-Dimensional Minimal Model of Frictional Rupture

The present study investigates rupture arrest using a minimal frictional rupture model that we developed in a previous study (Thøgersen et al., 2021). In this approach, the elastodynamic equations are reduced to a one-dimensional expression by assuming a block of finite height H in frictional contact along the plane $y = 0$, as presented in Figures 1c and 2. The displacement field is further taken constant along the z direction ($\partial_z u_i = 0$) during frictional ruptures that propagate along the x direction. Assuming that the rupture size L is always much larger than the system height ($L \gg H$), the elastodynamics can be solved in average over H to reduce momentum conservation into a one dimensional equation (Text S1 in Supporting Information S1). The resulting one-dimensional equation is expressed here in dimensionless units of space $\bar{x}$ and time $\bar{t}$, with the dot accent denoting a time derivative:

$$\ddot{\bar{u}} = \frac{\partial^2 \bar{u}}{\partial \bar{x}^2} - \Gamma \bar{\gamma} \bar{u} + \bar{\tau}. \tag{1}$$

Γ is a binary operator being respectively equal to one if Equation 1 describes a system with imposed-displacement boundary conditions at the top surface ($y = H$), or to zero if the system has imposed-stress at the top boundary. In the equation above, $\bar{u}(\bar{x}, \bar{t})$ is a scalar dimensionless displacement and $\bar{\tau}(\bar{x}, \bar{t})$ is a scalar dimensionless shear stress along the interface and defined as

$$\bar{\tau}(\bar{x}, \bar{t}) = \frac{\tau_0(\bar{x}) - \tau_f(\bar{x}, \bar{t})}{\sigma_n(\mu_s - \mu_k)}. \tag{2}$$

Here, $\bar{\tau}(\bar{x}, \bar{t})$ lumps the initial shear stress acting on the top of the block before the rupture τ_0, the frictional stress at the interface τ_f, the normal stress σ_n, the static μ_s and kinetic μ_k friction coefficients. The static friction

coefficient describes the magnitude of the shear stress that should be locally exceeded at the interface to initiate frictional sliding. The kinetic friction coefficient describes the residual frictional stress observed at the interface during sliding. More details about the boundary conditions are given in Text S1 in Supporting Information S1. The normal stress is assumed to be constant throughout the rupture, such that the model similarly applies to elastic-over-rigid and to symmetric frictional contact problems. The momentum equation, Equation 1, equivalently applies to in-plane (mode II) and out-of-plane (mode III) shear loading configurations, as summarized in Tables 1 and 2 and Table S1 in Supporting Information S1 that compile the definitions of variables.

In its simplest form, the model contains only two free parameters: (a) a dimensionless ratio of elastic moduli $\bar{\gamma}$ defined in Table 2, and (b) a spatial variable referred to as the dimensionless stress parameter in the manuscript

$$\bar{\tau}_k(\bar{x}) = \frac{\tau_0(\bar{x})/\sigma_n - \mu_k}{\mu_s - \mu_k}, \tag{3}$$

which corresponds to the value of $\bar{\tau}$ that will be observed once the frictional stress at the interface reaches kinetic friction associated to positive slip velocity. The definition of $\bar{\tau}_k$ allows for lumping spatial variations of initial stress and frictional parameters into a single variable. In the present study, we assume that variations of $\bar{\tau}_k$ results only from τ_0, but spatial variations of the other parameters (σ_n, μ_s, μ_k) can similarly be translated into a $\bar{\tau}_k(\bar{x})$ profile in the one-dimensional model with no loss of generality.

In the dimensionless form used in the model, static friction is observed as long as

$$\bar{\tau}_f\left(\bar{x},\bar{t}\right) = \bar{\tau}_k(\bar{x}) - \bar{\tau}\left(\bar{x},\bar{t}\right) < 1, \tag{4}$$

where $\bar{\tau}_f$ is the dimensionless frictional stress, as detailed in the Text S1 and Equation S13 in Supporting Information S1. Upon the onset of sliding, the frictional stress $\bar{\tau}_f\left(\bar{x},\bar{t}\right)$ locally drops from the static threshold ($\bar{\tau}_f = 1$) to residual friction ($\bar{\tau}_f = 0$) following the trajectory prescribed by a friction law. The simplest friction law, referred to in this paper as *Amontons-Coulomb* friction, assumes that the transition between static and kinetic friction is instantaneous upon sliding and requires no additional parameter. Frictional weakening often occurs by progressive energy dissipation during the approach to residual kinetic friction. In this paper, we follow the terminology defined by Tinti et al. (2005) and refer to the excess of work on top of residual friction as *breakdown work*. In this context, the total amount of breakdown work needed to weaken interfacial friction down to the residual stress is referred to as the *fracture energy* G_c and leads, in the dimensionless framework adopted in this paper, to the definition of a third dimensionless parameter:

$$\bar{G}_c = \frac{G_c\Lambda}{H\sigma_n^2(\mu_s - \mu_k)^2}, \tag{5}$$

with the elastic modulus Λ being defined in Table 2. A common first-order description of this process assumes that frictional weakening between μ_s and μ_k develops linearly with slip between $\bar{u} = 0$ and some critical slip distance $\bar{u} = \bar{d}_c$. This friction law will be referred to as *slip-weakening* in the manuscript and has the following dimensionless fracture energy: $\bar{G}_c = \bar{d}_c/2$. See Text S1 and Equations S13 and S14 in Supporting Information S1 for more details on the non-dimensional descriptions of Amontons-Coulomb and slip-weakening friction laws as well as on the origin of the scaling behind Equation S14 in Supporting Information S1.

2.1. The Crucial Role of Boundary Conditions on the Rupture Style

Following the definitions above, $\bar{\tau}_k$ corresponds to the value of $\bar{\tau}$ in Equation 1 observed once the shear stress (or friction) at the interface reaches its residual level. Postulating a steady-state solution and Amontons-Coulomb friction, Equation 1 reduces to the following ordinary differential equation within the rupture (i.e., within the sliding portion of the interface):

$$\left(\bar{v}_c^2 - 1\right)\frac{\partial^2\bar{u}}{\partial\bar{\xi}^2} = -\Gamma\bar{\gamma}\bar{u}(\xi) + \bar{\tau}_k(\xi), \tag{6}$$

with $\bar{\xi} = \bar{x} - \bar{v}_c\bar{t}$ being a co-moving coordinate following the rupture (i.e., the position of peak velocity) that moves at the propagation velocity $\bar{v}_c$.

Table 1
List of Variables Used in the Manuscript and the Supporting Information

List of main symbols	
$\bar{x}$	Position along the fault
$\bar{t}$	Time
$\bar{u}$	Slip
$\bar{\tau}$	Shear stress
$\bar{\tau}_f$	Frictional stress
Γ	Boundary conditions: imposed-stress ($\Gamma = 0$) or imposed-displacement ($\Gamma = 1$)
$\bar{\gamma}$	Elastic modulus parameter
$\bar{\tau}_k$	Dimensionless stress parameter
$\bar{G}_c$	Fracture energy
$\bar{d}_c$	Slip weakening distance
$\bar{K}$	One-dimensional stress intensity factor
$\bar{W}_b$	Breakdown work
$\bar{E}_{\text{el}}$	Elastic energy
$\bar{E}_{\text{kin}}$	Kinetic energy
$\bar{W}_{\text{ext}}$	External work
$\bar{v}_c$	Rupture propagation speed
$\bar{u}_p$	Final slip (i.e., after rupture arrest)
$\bar{\beta}$	Numerical damping
$\bar{\mathcal{L}}$	Length of the domain
$\bar{L}$	Rupture length
$\bar{L}_{\text{arr}}$	Arrest length
$\bar{L}^*_{\text{arr}}$	Smallest fracture energy barrier that can arrest a rupture
$\bar{G}^*_c$	Largest fracture energy that sustains steady rupture propagation
$\bar{\delta}$	$=2-\left(\bar{G}_c/\bar{G}^*_c\right)/\left(1+\sqrt{1-\bar{G}_c/\bar{G}^*_c}\right)$, see Equation 23
u_i	Displacement
$\hat{u}_0$	Imposed displacement at the top boundary
$\langle u_i \rangle$	Average displacement over the block height
σ_{ij}	Cauchy stress tensor
σ_n	Normal stress at the interface
τ_f	Frictional (shear) stress at the interface
H	Height of the solid block
λ	Lamé first coefficient
$\mathcal{G}$	Shear modulus
Λ	$=\lambda + 2\mathcal{G}$ for mode II or $=\mathcal{G}$ for mode III rupture
ρ	Solid density
μ_s	Static friction coefficient
μ_k	Kinetic friction coefficient

Note. The dashed line separates the dimensionless variables (above) and the variables with dimensions (below). See also Table 2 for further information on how to relate these variables to dimensional quantities.

Thøgersen et al. (2021) investigated steady-state rupture solutions governed by Equation 6 and revealed the crucial role of boundary conditions on the rupture style and its stability. For imposed-stress boundary condition ($\Gamma = 0$), the system promotes crack-like rupture and no steady-state pulse solution exists. Pulse-like rupture can be produced under the specific condition ($\bar{\tau}_k = 0$), which reduces Equation 6 to a one-dimensional wave equation.

Table 2
Summary of the Non-Dimensionalization Procedure Used in the Present Study

Physical quantities	Variables	Mode II rupture	Mode III rupture
Characteristic wave speed	$c = \sqrt{\frac{\Lambda}{\rho}}$	$\sqrt{\frac{\lambda+2\mathcal{G}}{\rho}}$	$\sqrt{\frac{\mathcal{G}}{\rho}}$
Characteristic displacement	$U = H\sigma_n \frac{\mu_s-\mu_k}{\Lambda}$	$H\sigma_n \frac{\mu_s-\mu_k}{\lambda+2\mathcal{G}}$	$H\sigma_n \frac{\mu_s-\mu_k}{\mathcal{G}}$
Characteristic time	$T = \sqrt{\frac{H^2\rho}{\Lambda}}$	$\sqrt{\frac{H^2\rho}{\lambda+2\mathcal{G}}}$	$\sqrt{\frac{H^2\rho}{\mathcal{G}}}$
Dimensionless distance	$\bar{x}$	$\frac{x}{H}$	$\frac{x}{H}$
Dimensionless displacement	$\bar{u} = \frac{\langle u_i \rangle_y}{U}$	$\frac{\langle u_x \rangle_y}{U}$	$\frac{\langle u_z \rangle_y}{U}$
Dimensionless shear stress	$\bar{\tau} = \frac{T^2}{\rho U H}(\tau_0 - \tau_f)$	$\frac{\sigma_{xy}/\sigma_n - \tau_f/\sigma_n}{\mu_s-\mu_k}$	$\frac{\sigma_{yz}/\sigma_n - \tau_f/\sigma_n}{\mu_s-\mu_k}$
Dimensionless stiffness	$\bar{\gamma} = \frac{2\mathcal{G}}{\Lambda}$	$\frac{2\mathcal{G}}{\lambda+2\mathcal{G}}$	2

Note. The elastic parameter Λ is equal to $\lambda + 2\mathcal{G}$ for Mode II rupture, and $\mathcal{G}$ for Mode III rupture.

Such pulse solutions have no specific shape and are unstable, as a local perturbation in the stress or interface conditions $\delta\bar{\tau}_k$ either stops the pulse (if $\delta\bar{\tau}_k < 0$) or expands it into a crack (if $\delta\bar{\tau}_k > 0$). Such unstable dynamics is reminiscent of the behavior of pulse-like ruptures between two semi-infinite elastic solids that have been reported in the literature for different type of friction laws (Brantut et al., 2019; Brener et al., 2018; Gabriel et al., 2012).

Conversely, imposed-displacement boundary condition ($\Gamma = 1$) enables stable pulse solutions for $\bar{\tau}_k > 0$. Under uniform pre-stress conditions, corresponding to constant $\bar{\tau}_k$, Equation 6 allows a steady-state pulse solution with width $\bar{\omega}$ and the following slip profile:

$$\bar{u}(\bar{\xi}) = \frac{\bar{\tau}_k}{\bar{\gamma}}\left(1 - \sin\left(\pi\bar{\xi}/\bar{\omega}\right)\right), \tag{7}$$

for $\bar{\xi} \in \left[-\bar{\omega}/2, \bar{\omega}/2\right]$. From the equation above, the final slip, $\bar{u}_p$, reached behind the steady-state pulse rupture corresponds to:

$$\bar{u}_p = 2\bar{\tau}_k/\bar{\gamma}. \tag{8}$$

Remarkably, this behavior is also in agreement with the stable pulse-like rupture that was reported in previous works studying finite elastic domains, where reflected elastic waves at the boundary interplay with the propagating rupture. This includes fault system with a damage zone with more compliant elastic properties (Idini & Ampuero, 2020) or earthquake rupture with a large aspect ratio (Weng & Ampuero, 2019). Interestingly, train of stable steady-state pulses can be produced also at the interface between unbounded elastic domains if an average slip velocity is imposed along the frictional plane instead of controlling the far-field stress (Roch et al., 2022). In our model, this second type of boundary condition ($\Gamma = 1$) corresponds then to large earthquake rupture, whose size saturates two representative dimensions of the fault systems, as depicted in Figure 1. Thøgersen et al. (2021) discusses in details the properties of slip pulses in our one-dimensional model.

2.2. The Arrest of Frictional Rupture in the One-Dimensional Model

The one-dimensional model (Equation 1) used in the present study contains two free parameters for Amontons-Coulomb friction ($\bar{\gamma}$, $\bar{\tau}_k$) and an additional third parameter $\left(\bar{G}_c\right)$ for slip-weakening friction. $\bar{\gamma}$ characterizes the elastic properties of the medium that are assumed to be macroscopically homogeneous and remains constant in the derivation of the model. Hence, a propagating rupture in the one-dimensional model can either be arrested by variations of $\bar{\tau}_k$ or $\bar{G}_c$. The former accounts for the level of shear stress existing in the system prior the rupture. A sharp reduction of $\bar{\tau}_k$ can stop a propagating rupture and corresponds to a *stress barrier*. Moreover, the initial finite amount of strain energy available in the surrounding bulk of thickness H scales as the square of τ_0 and is therefore increasing with $\bar{\tau}_k$. In the one-dimensional system, $\bar{\tau}_k$ describes the difference between external shear stress and the lowest value of frictional stress during sliding. If $\bar{\tau}_k$ is negative, this implies that the work injected by the external shear stress would be locally smaller than the frictional dissipation at residual friction and, therefore, a frictional rupture would absorb energy instead of releasing it. Hence, frictional ruptures in our one-dimensional model are energetically admissible only if somewhere along the interface

$$\bar{\tau}_k \geq 0. \tag{9}$$

Note that Equation 9 is a necessary condition for frictional rupture in the one-dimensional model but is not sufficient. It only guarantees rupture propagation once it has been nucleated. A gradual decay of $\bar{\tau}_k$ as one moves away from the nucleation site can then lead to the rupture arrest by a *depletion of available energy* in the system. Conversely, $\bar{G}_c$ describes the energy required to transform the interfacial shear conditions from static to kinetic friction. An increase in $\bar{G}_c$ corresponds to a *fracture energy barrier* and can also arrest a propagating rupture. In Sections 3 and 4, we simulate and study theoretically pulse- and crack-like rupture dynamics for these different arrest scenarios. Further in Section 5, we discuss how variations of physical conditions along natural fault systems can be expressed in terms of spatial variations of $\bar{\tau}_k$ and $\bar{G}_c$.

3. Numerical Simulations of Frictional Rupture Arrest

Here, Equation 1 is solved numerically using a finite difference scheme with uniform grid size $\Delta\bar{x}$ and Euler-Cromer (Cromer, 1981) time-integration scheme with time step $\Delta\bar{t}$, as described in Thøgersen et al. (2021). At each grid point i and time step, the interface can be either stuck $(\dot{\bar{u}}_i = 0)$ or slipping $(\dot{\bar{u}}_i \neq 0)$. Static equilibrium in the stuck region, that is, Equation 1 with $\ddot{\bar{u}} = 0$, leads in combination with the criterion of Equation 4 to the following inequality

$$\frac{\bar{u}_{i+1} - 2\bar{u}_i + \bar{u}_{i-1}}{(\Delta\bar{x})^2} - \Gamma\bar{\gamma}\bar{u}_i + \bar{\tau}_{k,i} < 1. \tag{10}$$

Conversely, the dynamics of the sliding portions of the interface is integrated from Equation 1 as:

$$\ddot{\bar{u}}_i = \frac{\bar{u}_{i+1} - 2\bar{u}_i + \bar{u}_{i-1}}{(\Delta\bar{x})^2} - \Gamma\bar{\gamma}\bar{u}_i + \bar{\tau}_i + \bar{\beta}\frac{\dot{\bar{u}}_{i+1} - 2\dot{\bar{u}}_i + \dot{\bar{u}}_{i-1}}{(\Delta\bar{x})^2}, \tag{11}$$

where the scalar $\bar{\beta}$ is a small numerical parameter used to damp spurious high-frequency oscillations and is set to the standard value of $\bar{\beta} = \sqrt{0.1}\Delta\bar{x}$ (Amundsen et al., 2012; Knopoff & Ni, 2001). The set of Equations 10 and 11 is closed by the friction law that describes the evolution of $\bar{\tau}_i$ according to Equation S13 in Supporting Information S1. More details about the convergence and parameters of the numerical scheme are provided Text S2 in Supporting Information S1.

The initial condition of every simulation corresponds to an interface entirely stuck under a given initial shear stress defined by $\bar{\tau}_k(\bar{x})$. The domain has a finite length $\bar{\mathcal{L}}$ and the boundary conditions on the left and the right edges correspond to $\bar{u}(0) = 0$ and $\bar{u}(\bar{\mathcal{L}}) = 0$. In this study, we focus on rupture propagating from the left to the right of the domain. Rupture nucleation is triggered by defining a region of higher shear stress at the left edges with $\bar{\tau}_k(0) = 1$. Such configuration is depicted in Figure 1c and describes rupture nucleation beyond a barrier (as for instance in Gvirtzman and Fineberg (2021)); however other nucleation processes could be considered with no loss of generality.

Figure 3 summarizes the different arrest scenarios and the simulated frictional slip observed after a pulse-like and crack-like rupture. A first set of simulations compares results for the different rupture styles under homogeneous pre-stress and fracture energy (Figure 3a): a steady-state pulse-like rupture arises with slip occurring within a propagating patch of constant width and amplitude. In contrast, when rupture propagates as a crack, the entire ruptured zone keeps sliding during the whole simulation duration, such that both the size and the amplitude of the slip rate profile increase with propagation time. Figures 3b–3d summarize the evolution of frictional slip during pulse-like and crack-like ruptures, but testing inhomogeneous conditions. Because $\bar{\tau}_k$ describes the excess of shear pre-stress on top of residual friction, a sharp drop of $\bar{\tau}_k$ toward negative value corresponds to a stress barrier and is presented in Figure 3b. Frictional weakening during rupture can also involve additional energy dissipation, which in our dimensionless model is governed by $\bar{G}_c$. A fracture energy barrier can then be simulated by a sharp increase in $\bar{G}_c$ above some critical value $\bar{G}_c^*$, as presented in Figure 3c. $\bar{G}_c^*$ corresponds to the largest dimensionless fracture energy for which steady rupture propagation is sustainable and is quantitatively described in Section 4 below. Finally, frictional ruptures can stop by running out of available energy in the system, which is function of the initial shear stress and whose depletion can be modeled by a progressive decay of $\bar{\tau}_k$, as presented in Figure 3d.

The comparison of rupture styles in Figure 3 sheds light on the significant difference in terms of final slip that exists between the two frictional rupture modes. Most notably, the profile of slip observed after a pulse-like rupture is much more sensitive to the arrest scenarios and keeps a precise record of the local variations of bulk and interface conditions compared to the profile of slip observed after crack-like rupture.

4. Theoretical Predictions of the Arrest of Pulse- and Crack-Like Ruptures

4.1. Equivalence to the Burridge-Knopoff Approach

The one-dimensional model expressed in its discretized form in Equations 10 and 11 is equivalent to Burridge-Knopoff type of models widely used in the literature to describe earthquakes rupture and statistics (e.g., Braun et al., 2009; Brown et al., 1991; Burridge and Knopoff, 1967; Carlson et al., 1994; Olami et al., 1992;

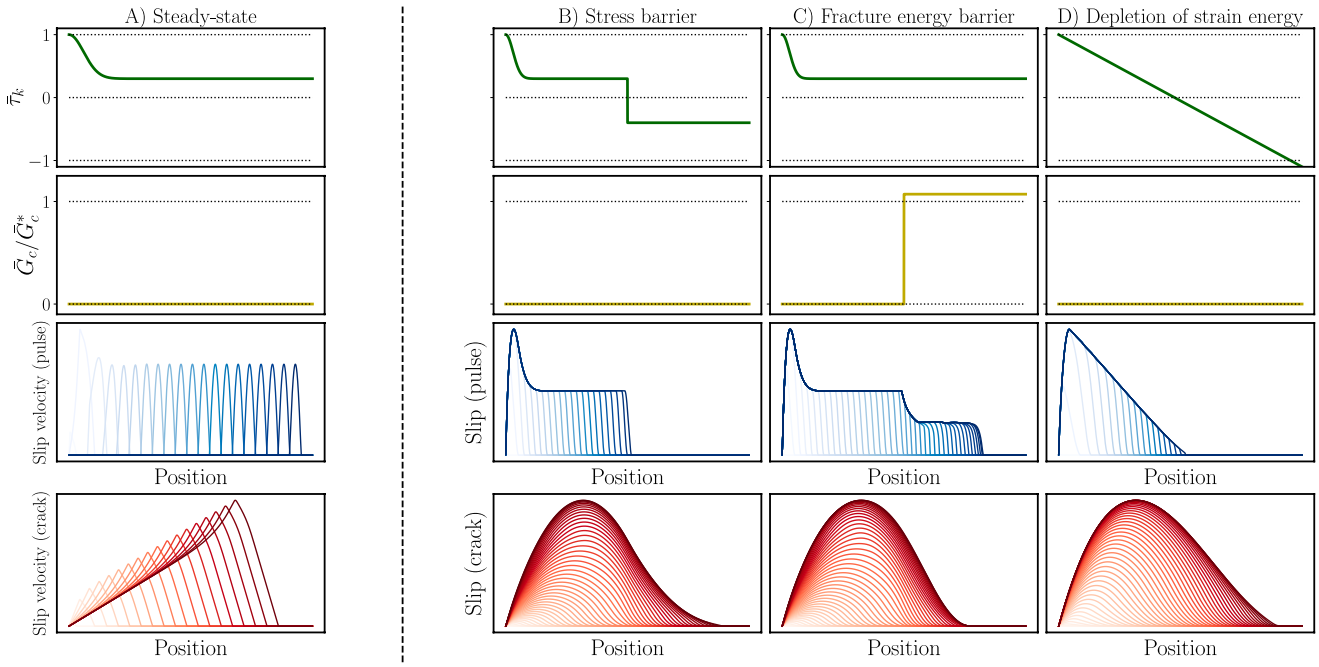

Figure 3. Slip velocities and three arrest scenarios studied in the present study with the resulting final slip profiles observed after a pulse-like (blue) and a crack-like (red) rupture. Slip velocities and slip profiles are calculated by solving numerically Equation 1. In each column, the top two panels display the initial profiles of $\bar{\tau}_k$ and $\bar{G}_c$ along the interface. Rupture is nucleated by a larger value of pre-stress located near $\bar{x} = 0$. (a) Steady-state slip velocities for pulse-like and crack-like ruptures. The increasing color shade of each profile indicates progression in time. (b) A sharp drop of $\bar{\tau}_k$ forms a stress barrier that arrests frictional rupture. (c) The frictional rupture is arrested by a sharp increase in $\bar{G}_c$ that corresponds to a fracture energy barrier. (d) A linear decay of $\bar{\tau}_k$ progressively reduces the available strain energy to propagate the frictional rupture and eventually arrests it.

Trømborg et al., 2014). Starting from the seminal work of Burridge and Knopoff (1967), the Burridge-Knopoff model for earthquakes consists of a horizontal array of blocks with identical mass connected by longitudinal springs. Each block is submitted to a normal force and resists horizontal sliding by friction. The system is either loaded by applying a lateral forces or by connecting each block to a moving support via vertical springs, often referred to as leaf springs. Our one-dimensional formulation of Equation 11 can be obtained from Burridge-Knopoff models by setting blocks mass to unity, lateral springs stiffness to $(\Delta\bar{x})^{-2}$, and the leaf springs stiffness to $\bar{\gamma}$. This analogy is exploited later in the present study to derive pulse and crack equations inspired from Burridge-Knopoff models. Our one-dimensional model represents therefore an interesting framework to bridge the discrete description of earthquake dynamics provided in Burridge-Knopoff models to continuum models of faults. The main difference of our approach is that we introduce here a characteristic length scale H, that does not exist in Burridge-Knopoff models. The implications of this additional length scale in our model is further discussed in Section 5.1 below.

4.2. One-Dimensional Energy Balance

The different contributions to the energy balance of the one-dimensional system correspond to the *elastic energy* $\bar{E}_{\text{el}}$, the *kinetic energy* $\bar{E}_{\text{kin}}$, and the *external work* $\bar{W}_{\text{ext}}$. During the frictional rupture, the work done by the external forces is converted into internal energy such that: $\bar{W}_{\text{ext}} = \bar{E}_{\text{el}} + \bar{E}_{\text{kin}}$. In analogy to Burridge-Knopoff models with $\mathcal{N}$ blocks, the elastic energy corresponds to the potential energy stored in the longitudinal springs and the leaf springs:

$$\bar{E}_{\text{el}} = \sum_{1}^{\mathcal{N}-1} \frac{1}{2}(\Delta\bar{x})^{-2}(\bar{u}_{i+1} - \bar{u}_i)^2 + \Gamma \sum_{1}^{\mathcal{N}} \frac{1}{2}\bar{\gamma}\bar{u}_i^2 \tag{12}$$

or in the continuum form

$$\bar{E}_{\text{el}} = \frac{1}{2}\int_0^{\bar{\mathcal{L}}} \left(\frac{\partial\bar{u}}{\partial\bar{x}}\right)^2 d\bar{x} + \Gamma\frac{1}{2}\int_0^{\bar{\mathcal{L}}} \bar{\gamma}\bar{u}^2 d\bar{x}. \tag{13}$$

Note that the second right-hand-side contribution to the elastic energy in Equation 13 (i.e., the leaf springs in the Burridge-Knopoff model) only arises for imposed-displacement boundary condition ($\Gamma = 1$, pulses). Similarly, the kinetic energy corresponds to

$$\bar{E}_{\text{kin}} = \frac{1}{2}\int_0^{\bar{\mathcal{L}}} \left(\frac{\partial \bar{u}}{\partial \bar{t}}\right)^2 d\bar{x}. \tag{14}$$

The external work corresponds to

$$\bar{W}_{\text{ext}} = \int_0^{\bar{\mathcal{L}}} \left(\bar{\tau}_k \bar{u} - \bar{W}_b(\bar{u})\right) d\bar{x}. \tag{15}$$

From the definition of $\bar{\tau}_k$ in Equation 3, the first term on the right-hand side of Equation 15 combines the work of the external shear stress τ_0 and the work done against residual friction. The dimensionless breakdown work $\bar{W}_b$ accounts for additional dissipation on top of residual friction, which is zero for Amontons-Coulomb friction (see Equation S14 in Supporting Information S1) and is defined as

$$\bar{W}_b(\bar{u}) = \int_0^{\bar{u}} \bar{\tau}_f(\mathcal{U})\, \mathrm{d}\mathcal{U}, \tag{16}$$

with $\bar{\tau}_f(\bar{u})$ defined in Equation S13 in Supporting Information S1. The reader is referred to Cocco et al. (2023) and references therein for a review of the different definitions and partitions of frictional work used in seismology.

It is important to note that the initial level of internal energy in the one-dimensional system is set as zero $\left(\bar{E}_{\text{el}} + \bar{E}_{\text{kin}} = \bar{W}_{\text{ext}} = 0\right)$. Throughout the rupture, the variation of elastic strain energy into a three-dimensional solid of dimensions $\mathcal{L} \times H \times W$ is accounted for in the one-dimensional model by change in $\bar{W}_{\text{ext}}$ and $\bar{E}_{\text{el}}$. For the simplicity of the argument, let us assume Amontons-Coulomb friction and homogeneous slip along the horizontal extent $\bar{L}$ of a frictional rupture such that only the second right-hand-side term of Equation 13 contributes to the elastic energy. The amount of energy released by the rupture into the system corresponds to

$$\bar{E}_r = \bar{W}_{\text{ext}} - \bar{E}_{\text{el}} = \bar{L}\left(\bar{\tau}_k \bar{u} - \frac{1}{2}\Gamma \bar{\gamma} \bar{u}^2\right), \tag{17}$$

which is converted into kinetic energy. Frictional rupture is *energetically admissible* if $\bar{E}_r \geq 0$.

For imposed-stress boundary conditions ($\Gamma = 0$), frictional slip is admissible as long as $\bar{\tau}_k \geq 0$, and the larger the slip the more energy is released in the system. Conversely, for imposed-displacement boundary conditions ($\Gamma = 1$), part of the work injected by the pre-stress in the system goes into the leaf spring elastic energy, such that frictional slip is only admissible for $0 \leq \bar{u} \leq 2\bar{\tau}_k/\bar{\gamma}$, with the upper bound being equivalent to the steady-state slip solution of Equation 8. This different energy transfer between stress- and displacement-controlled conditions explains why, in the wake of the propagating rupture, the interface re-stick (i.e., pulse-like rupture) for $\Gamma = 1$ whereas sliding continues in the form of a crack-like rupture for $\Gamma = 0$. Physically, this one-dimensional energy balance describes the fact that the shear stress τ_0 remains constant in the three-dimensional solid during the rupture for imposed-stress boundary conditions, whereas τ_0 progressively drops with frictional slip if the displacement is imposed at the top surface of the block, according to Figure 2. This one-dimensional energy balance is exploited further in Texts S3 and S4 in Supporting Information S1 to describe frictional rupture beyond the homogeneous steady-state simplification in order to propose pulse and crack arrest equations which are summarized hereafter.

4.3. Pulse Arrest Equations

First, we follow the approach proposed by Elbanna and Heaton (2012) and derive a pulse equation by integrating the energy balance between the nucleation site $\bar{x} = 0$ and the leading tip of the pulse $\bar{x} = \bar{L}$. Next, we assume that the ruptured area is larger than the width of the pulse $\bar{L} \gg \bar{\omega}$ to neglect the contribution of the regions within the pulse width and obtain the following ordinary differential equation:

$$\frac{\partial^2 \bar{u}_p}{\partial \bar{x}^2} = \bar{\gamma}\bar{u}_p - 2\bar{\tau}_k + \frac{2\bar{W}_b(\bar{u}_p)}{\bar{u}_p}, \tag{18}$$

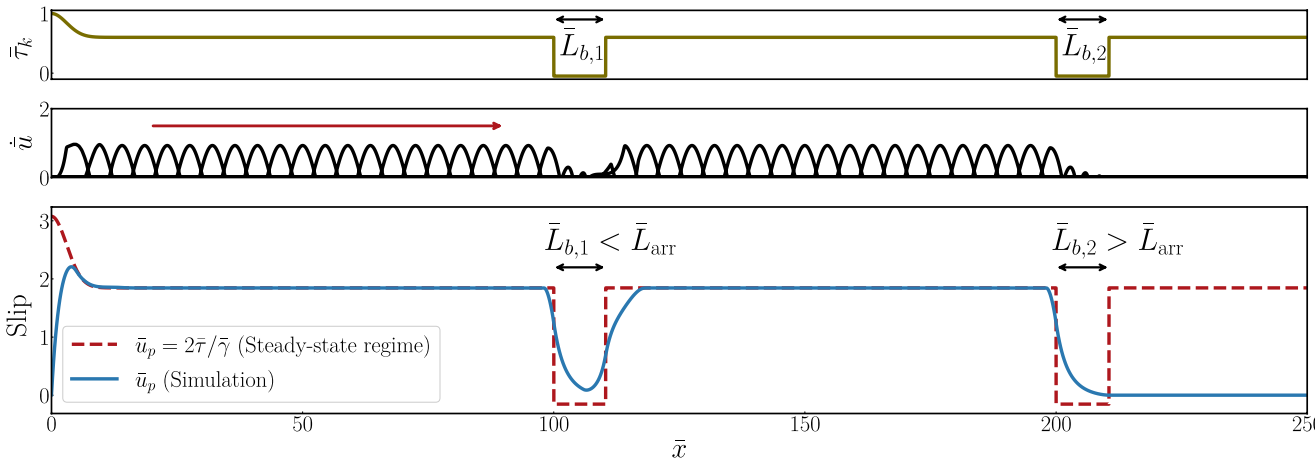

Figure 4. Example of slip pulse simulation. *Top*: Profile of the initial stress parameter, $\bar{\tau}_k$, with a Gaussian stress concentration introduced on the left side of the domain to nucleate frictional rupture. Stress barriers with similar amplitude $\bar{\tau}_{k,b} = -0.05$ but various lengths $\bar{L}_{b,i}$ are placed along the fault at $\bar{x} = 100$ and $\bar{x} = 200$. *Middle*: Snapshots of slip velocity at different time steps, showing slip pulse propagation in the direction of the red arrow. Note that the pulse crossed the first barrier, but was stopped by the longer second barrier. *Bottom*: Final slip profile compared to the steady-state regime. A propagating pulse can cross a barrier of length smaller than the arrest length $\bar{L}_{\text{arr}}$ but is arrested by a barrier that is larger than $\bar{L}_{\text{arr}}$.

with $\bar{u}_p$ being the final slip reached in the wake of the traveling pulse. The detailed derivation of Equation 18 can be found in the Text S3 in Supporting Information S1.

4.3.1. Stress Barriers

This arrest scenario is studied by simulating a steadily propagating pulse under a given initial stress $\bar{\tau}_{k,0}$ that reaches a region of lower pre-stress at $\bar{x} = \bar{x}_b$, as shown in Figure 4. If the shear stress within the barrier $\bar{\tau}_{k,b}$ is still positive, a steady-state pulse solution exists and the final slip evolves toward the new steady-state according to Equation 8. If $\bar{\tau}_{k,b}$ is negative (as in Figure 4), sustained pulse propagation is no longer possible such that the rupture will be arrested by barriers that exceed a critical length defined as $\bar{L}_{\text{arr}}$. The pulse Equation 18 can be used to predict the decay of slip observed in Figure 4 within a barrier of negative pre-stress. For negligible breakdown work (i.e., Amontons-Coulomb friction with $\bar{W}_b = 0$), the general solution of Equation 18 is the sum of two exponential functions. As shown in Figure S2 in Supporting Information S1, the pulse arrest Equation 18 can be used to derive different predictions of the decay of frictional slip within the barrier from its initial steady-state value $\bar{u}_p = 2\bar{\tau}_k/\bar{\gamma}$. For instance, the following solution is obtained by searching for solution where both $\bar{u}_p(\bar{x}')$ and its first derivative are equal to zero at the arrest location:

$$\bar{u}_p(\bar{x}') = \frac{-2\bar{\tau}_{k,b}}{\bar{\gamma}}\left(\cosh\left(\left(\bar{x}' - \bar{L}_{\text{arr}}\right)\sqrt{\bar{\gamma}}\right) - 1\right), \tag{19}$$

with $\bar{x}' = \bar{x} - \bar{x}_b$, where $\bar{x}_b$ is the position at which the barrier starts. Remembering that $\bar{\tau}_{k,b} < 0$, the equation above has a positive root $\bar{u}_p\left(\bar{x}' = \bar{L}_{\text{arr}}\right) = 0$ which can be used to predict the arrest length:

$$\bar{L}_{\text{arr}}(\bar{\tau}_{k,0}; \bar{\tau}_{k,b}) = \bar{\gamma}^{-\frac{1}{2}} \operatorname{arccosh}\left(\frac{\bar{\tau}_{k,0} - \bar{\tau}_{k,b}}{-\bar{\tau}_{k,b}}\right). \tag{20}$$

Figure 5a compares this theoretical prediction with the numerical simulations for various stress barriers ($-\bar{\tau}_{k,b}$) with different initial pre-stress ($\bar{\tau}_{k,0}$) and moduli $\bar{\gamma}$. The theoretical prediction of Equation 20 captures well the trend observed in the simulations but systematically underestimates the simulated arrest length. This underestimation is explained by the assumptions used to derive the pulse arrest Equation 18, which assume infinitesimal pulse width and neglect the contribution of kinetic energy contained within the pulse (see detailed derivation Text S3 in Supporting Information S1). As shown in Figure S2 in Supporting Information S1, the finite width of the pulse also has an effect on the decay of the frictional slip, which starts before the position of the barrier and that the prediction (Equation 20) neglects.

4.3.2. Fracture Energy Barriers

If the contribution of the breakdown work is non-negligible (as with slip-weakening friction), two end-member situations can occur. In a first case, frictional weakening is complete in the wake of the rupture, such that the

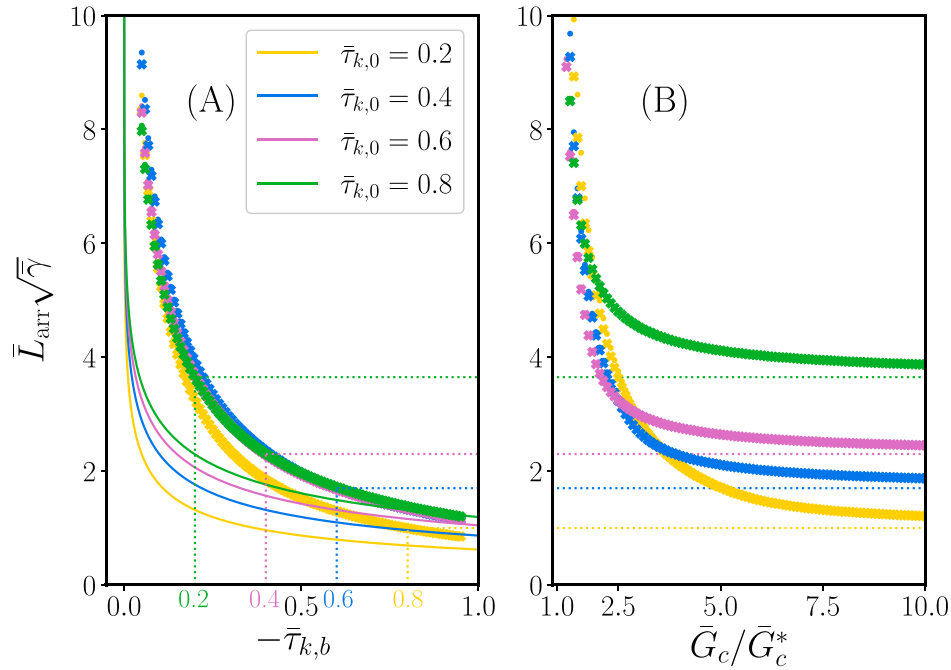

Figure 5. Arrest length for slip pulse in presence of stress (a) and fracture energy (b) barriers. The solid lines on the plot (a) correspond to the theoretical prediction given by Equation 20. Color symbols correspond to simulation results at different initial stresses $\bar{\tau}_{k,0}$ for $\bar{\gamma} = 0.65$ (circle) and $\bar{\gamma} = 2.0$ (cross). The dashed horizontal lines highlight how the stress barrier with amplitude $\bar{\tau}_{k,b} = \bar{\tau}_{k,0} - 1$ gives the asymptotic value of the arrest length, that is, $\bar{L}^*_{\mathrm{arr}}$ in Equation 25, for large dimensionless fracture energy $\bar{G}_c \gg \bar{G}^*_c$.

breakdown work is constant and equates the fracture energy $\bar{W}_b = \bar{G}_c$. Equation 18 is a non-linear ordinary differential equation, but the possibility for smoothly traveling pulse can nevertheless be investigated by neglecting the second-order derivative, which leads to the following slip solution behind the traveling pulse:

$$\bar{u}_p = \frac{\bar{\tau}_k}{\bar{\gamma}}\left(1 + \sqrt{1 - \frac{2\bar{G}_c\bar{\gamma}}{\bar{\tau}_k^2}}\right). \tag{21}$$

Note how Equation 21 leads to the steady-state solution for Amontons-Coulomb friction of Equation 8 as $\bar{G}_c \to 0$. Interestingly, neglecting the contribution of the fracture energy in the steady-state pulse solution leads to an overestimation of the final slip by at most a factor two. The solution Equation 21 leads to the definition of a critical value of $\bar{G}_c$, above which sustained pulse propagation is no longer admissible:

$$\bar{G}^*_c = \frac{\bar{\tau}_k^2}{2\bar{\gamma}}. \tag{22}$$

Plugging Equation 21 into the pulse Equation 18, one can define $\bar{\delta}$ as

$$\frac{\partial^2 \bar{u}_p}{\partial \bar{x}^2} = \bar{\gamma}\bar{u}_p - 2\bar{\tau}_k + \frac{2\bar{G}_c}{\bar{u}_p} = \bar{\gamma}\bar{u}_p - \bar{\tau}_k\left(2 - \frac{\bar{G}_c/\bar{G}^*_c}{1 + \sqrt{1 - \bar{G}_c/\bar{G}^*_c}}\right) \equiv \bar{\gamma}\bar{u}_p - \bar{\delta}\bar{\tau}_k, \tag{23}$$

with $1 \le \bar{\delta} \le 2$ being a parameter that only depends on the interface fracture energy. For the largest admissible fracture energy (corresponding to $\bar{G}_c = \bar{G}^*_c$), one has $\bar{\delta} = 1$, whereas for zero fracture energy $\bar{\delta} = 2$.

As in the case of stress barriers, an increase in fracture energy given by $\bar{G}_c > \bar{G}^*_c$ will arrest the rupture if its length is larger than some arrest length $\bar{L}_{\mathrm{arr}}$. This leads to the other situation for which frictional weakening is incomplete in the wake of the rupture $\left(\bar{W}_b < \bar{G}_c\right)$. The integration of the breakdown work for the slip

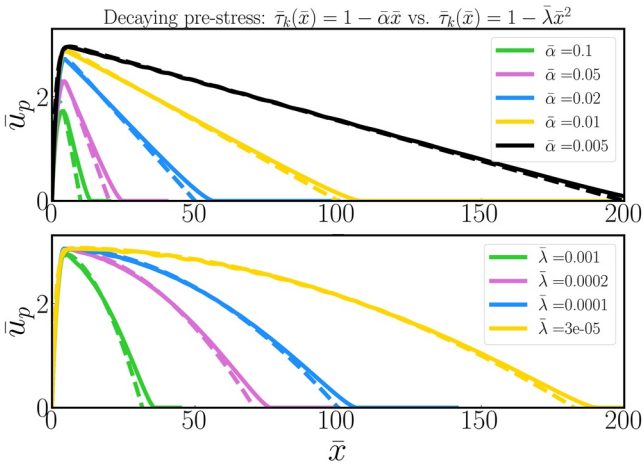

Figure 6. Profile of final slip caused by a pulse-like rupture propagating toward a region with decaying pre-stress: simulations (solid lines) versus the analytical predictions (dashed-lines) derived from the pulse arrest Equation 18. Top: Linearly decaying pre-stress with final slip predicted by Equation 26. Bottom: Quadratically decaying pre-stress with final slip predicted by Equation 27.

weakening law (see Equation S14 in Supporting Information S1) leads to the following ordinary differential equation:

$$\frac{\partial^2 \bar{u}_p}{\partial \bar{x}^2} = \left(\bar{\gamma} - \frac{1}{2\bar{G}_c}\right)\bar{u}_p - 2(\bar{\tau}_k - 1). \tag{24}$$

For very large $\bar{G}_c$, the equation above tends to the one describing a stress barrier with $\bar{\tau}_{k,b} = \bar{\tau}_k - 1$. Physically, this means that there is not enough slip and energy to drive the weakening of the interface within the barrier such that frictional stress stays close to its static value (corresponding to $\bar{\tau} = \bar{\tau}_k - 1$) throughout the width of the pulse. An important implication is that any fracture energy barrier with a length shorter than $\bar{L}^*_{\text{arr}}$ cannot stop a propagating slip pulse regardless of its fracture energy amplitude:

$$\bar{L}^*_{\text{arr}}(\bar{\tau}_k) = \bar{L}_{\text{arr}}(\bar{\tau}_{k,0} = \bar{\tau}_k; \bar{\tau}_{k,b} = \bar{\tau}_k - 1), \tag{25}$$

with $\bar{L}_{\text{arr}}$ being defined in Equation 20. Figure 5b presents the two asymptotic situations that describe the arrest of pulse-like rupture by a fracture energy barrier: $\bar{L}_{\text{arr}}$ diverges as $G_c \to \bar{G}^*_c$, whereas for $G_c \to \infty$ the arrest length converges toward $\bar{L}^*_{\text{arr}}(\bar{\tau}_k)$.

4.3.3. Progressive Decay of Available Strain Energy

Ruptures can also be arrested by smoothly decaying pre-stress, $\bar{\tau}_k$. Indeed, earthquakes typically nucleate in a critically stressed portion of a fault before reaching sub-critically stressed regions. In the one-dimensional model, stress criticality is described by the dimensionless variables $\bar{\tau}_k$ (with critical values corresponding to $\bar{\tau}_k > 1$). Pulse rupture in a smoothly decaying pre-stress can be described using the pulse arrest equation. For example, with a linearized decaying profile of the form $\bar{\tau}_k(\bar{x}) = 1 - \bar{\alpha}\bar{x}$, the following final slip profile satisfies Equation 18:

$$\bar{u}_p = \frac{2}{\bar{\gamma}}\left(1 - \bar{\alpha}\bar{x} - \exp\left(-\bar{x}\sqrt{\bar{\gamma}}\right)\right). \tag{26}$$

Similarly, for a quadratic decay of the pre-stress profile of the form $\bar{\tau}_k = 1 - \bar{\lambda}\bar{x}^2$, the following profile of slip can be predicted using the pulse equation:

$$\bar{u}_p = \frac{2}{\bar{\gamma}}\left(\left(1 - 2\bar{\lambda}\bar{\gamma}^{-1}\right)\left(1 - \exp\left(-\bar{x}\sqrt{\bar{\gamma}}\right)\right) - \bar{\lambda}\bar{x}^2\right). \tag{27}$$

Figure 6 validates the theoretical predictions (Equations 26 and 27) derived from the pulse equation with numerical simulations. Accounting for the contribution of the growing exponential term $\sim\exp\left(\bar{x}\sqrt{\bar{\gamma}}\right)$, which was neglected in the derivation of Equations 26 and 27, could further improve the predicted slip closed to the arrest position.

For slowly decaying pre-stress (i.e., $\bar{\alpha}; \bar{\lambda} \ll 1$), both Equations 26 and 27 predict that the rupture arrests at the location where $\bar{\tau}_k = 0$, which leads to $\bar{L}_{\text{arr}} \cong \bar{\alpha}^{-1}$ and $\bar{L}_{\text{arr}} \cong \bar{\lambda}^{-1/2}$, respectively for the linear and quadratic pre-stress. In dimensional units, the rupture is then expected to arrest where the initial shear stress τ_0 becomes smaller than residual friction $\mu_k\sigma_n$.

After nucleation, the rapid slip rise is governed by elasticity and the exponential term $\left(1 - \exp\left(-\bar{x}\sqrt{\bar{\gamma}}\right)\right)$. Post peak, the slow decay mimics the profile of initial stress and is governed by the linear term of Equation 26 or the quadratic decay in Equation 27.

4.4. Crack Arrest Equations

Crack-like ruptures in Burridge-Knopoff models have received more attention in the literature compared to pulses. Past works (e.g., Amundsen et al., 2012; Trømborg et al., 2011) showed that the arrest of cracks in these models can be well predicted using the net shear force acting on the sliding block just ahead of the propagating tip, which corresponds, in our one-dimensional setup, to the following integral:

$$\bar{K}(\bar{L}) = \int_0^{\bar{L}} \bar{\tau}_k(\bar{x})\,\mathrm{d}\bar{x}. \tag{28}$$

Crack-like ruptures have different energy budget than pulses. First, kinetic energy during the rupture is not concentrated near the propagating tip but spreads over the entire ruptured area. Second, there is no contribution from the leaf spring elastic energy because $\Gamma = 0$ in Equation 13. Therefore, the work done by the external stress $\bar{W}_{\text{ext}}$ is converted into elastic and kinetic energy within the crack and corresponds to the energy released by the rupture.

To illustrate the difference of energy budget governing pulse and crack dynamics, we derive the steady-state solution for a propagating crack under homogeneous conditions in Supporting Information S1 (see Text S4.1 and Figure S3 in Supporting Information S1). Using this steady-state solution, we can compute the energy released by the rupture, which corresponds to

$$\bar{E}_{\text{crack}} = \frac{\bar{\tau}_k^2 \bar{L}^3}{6\bar{v}_c(\bar{v}_c + 1)} \tag{29}$$

for a crack of size $\bar{L}$ propagating at speed $\bar{v}_c$. For homogeneous conditions, $K\left(\bar{L}\right) = \bar{\tau}_k \bar{L}$ can then be related to $\bar{E}_{\text{crack}}$ by expressing the rate of energy release per unit crack advance, $\bar{G}$:

$$\bar{G}\left(\bar{L}, \bar{v}_c\right) = \frac{\mathrm{d}\bar{E}_{\text{crack}}}{\mathrm{d}\bar{L}} = \frac{\bar{\tau}_k^2 \bar{L}^2}{2\bar{v}_c(\bar{v}_c + 1)} = \bar{K}^2 \bar{\mathcal{A}}(\bar{v}_c). \tag{30}$$

By analogy with dynamic fracture mechanics (e.g., Freund, 1998), $\bar{K}$ and $\bar{G}$ correspond to the one-dimensional stress intensity factor and the energy release rate, whereas $\bar{\mathcal{A}}$ is some universal function of the rupture speed.

4.4.1. Stress Barriers

For a stress barrier, the arrest location of crack-like rupture is well predicted by the first position along the crack path where the net force acting on the sliding element ahead of the tip becomes zero (Amundsen et al., 2012; Trømborg et al., 2011). Using Equation 28, the predicted arrest length $\bar{L}_{\text{arr}}$ of crack-like rupture in the one-dimensional model can be readily defined as $\bar{K}\left(\bar{x}_b + \bar{L}_{\text{arr}}\right) = 0$, which implies that

$$\bar{L}_{\text{arr}}(\bar{\tau}_k; \bar{\tau}_{k,0}; \bar{x}_b) = -\frac{\bar{x}_b \bar{\tau}_{k,0}}{\bar{\tau}_{k,b}}, \tag{31}$$

recalling that $\bar{\tau}_{k,b}$ has to be negative to form a stress barrier. Unlike pulse-like rupture (see Equation 20), the arrest length of crack also depends on the position of the barrier $\bar{x}_b$. This is explained by the fact that the energy released by a crack depends on its size $\bar{L}$ to a cubic power (see Equation 29), whereas the energy released by a steadily propagating pulse is constant and only depends on $\bar{\tau}_k$ (see Equation S36 and Text S3.4 in Supporting Information S1 for more details).

4.4.2. Fracture Energy Barriers

As discussed in the context of pulses, the two characteristic quantities $\bar{G}_c^*$ and $\bar{L}_{\text{arr}}^*$ can be similarly defined for cracks. $\bar{G}_c^*$ corresponds to the minimal amount of dimensionless fracture energy required to arrest the rupture (sustained rupture growth is admissible for $\bar{G}_c < \bar{G}_c^*$). $\bar{L}_{\text{arr}}^*$ corresponds to the minimum barrier length required to arrest the rupture (no fracture energy barrier with size $\bar{L}_{\text{arr}} < \bar{L}_{\text{arr}}^*$ can arrest a propagating rupture). The main difference is that for crack-like rupture both $\bar{G}_c^*$ and $\bar{L}_{\text{arr}}^*$ also depend on the size of the crack when it reaches the barrier $\left(\bar{L} = \bar{x}_b\right)$.

As in the case of pulse-like rupture, $\bar{L}_{\text{arr}}^*$ corresponds to the arrest length caused by a stress barriers with $\bar{\tau}_{k,b} = \bar{\tau}_k - 1$, which leads to the following expression using Equation 31

$$\bar{L}_{\text{arr}}^*(\bar{\tau}_k; \bar{x}_b) = \frac{\bar{x}_b \bar{\tau}_k}{1 - \bar{\tau}_k}. \tag{32}$$

As discussed for pulse-like rupture, $\bar{L}_{\text{arr}}^*$ above governs rupture arrest in the asymptotic limit $\bar{G}_c \to \infty$, for which frictional weakening is limited and $\bar{\tau}_f$ stays near the static value.

The other end-member situation corresponds to fully developed frictional weakening such that $\bar{W}_b = \bar{G}_c = \bar{d}_c/2$. The one-dimensional dynamic fracture energy balance $\left(\bar{G} = \bar{G}_c\right)$ can be used together with Equation 30 to define critical fracture energy following the derivation detailed in Text S4 in Supporting Information S1:

$$\bar{G}_c^*(\bar{\tau}_k; \bar{x}_b) = \frac{8\left(1 - \bar{\tau}_k^2\right)\bar{x}_b^2}{9}\left(1 - \sqrt{1 - \bar{\tau}_k^2}\right). \tag{33}$$

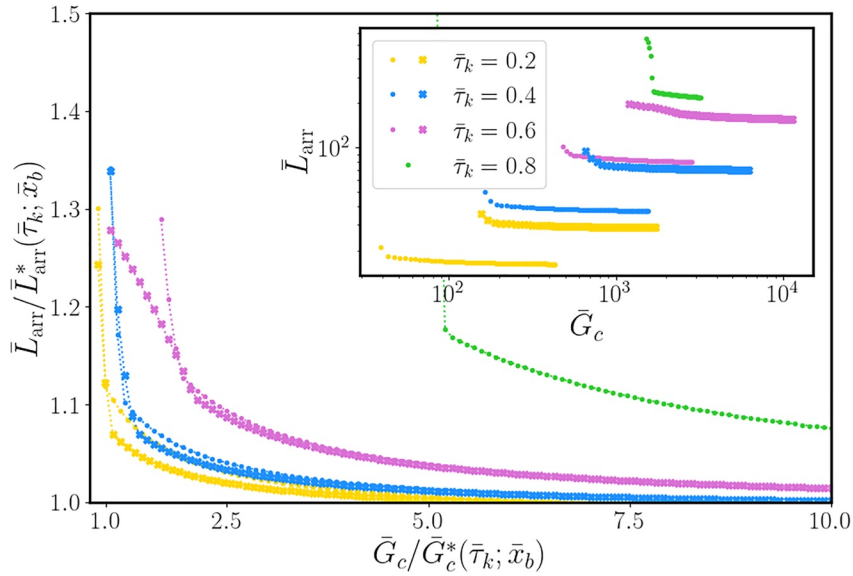

Figure 7. Arrest length of crack-like rupture stopped by a fracture energy barrier simulated for different values of initial stress parameter $\bar{\tau}_k$ and fracture energy $\bar{G}_c$. The markers identify simulations with barrier size $\bar{x}_b = 50$ (dots) and $\bar{x}_b = 100$ (crosses). The inset shows the raw data that spans several orders of magnitude in $\bar{L}_{\text{arr}}$ and $\bar{G}_c$, and that are collapsed in the main plot using the definitions of $\bar{G}^*_c$ in Equation 33 and $\bar{L}^*_{\text{arr}}$ in Equation 32.

Figure 7 tests the predictions of $\bar{L}^*_{\text{arr}}$ (Equation 32) and $\bar{G}^*_c$ (Equation 33) against simulations that span several orders of magnitude of fracture energy and arrest length. First, it shows that the simplifications behind Equation 33 gives an accurate prediction for moderate pre-stress. At large pre-stress, dynamical effects associated to fast crack speed tend to overshoot the prediction of $\bar{L}_{\text{arr}}$ in Equation S50 in Supporting Information S1 and, thereby, $\bar{G}^*_c$. Second, the arrest of crack-like rupture is much sharper than in the case of slip pulse, such that $\bar{L}^*_{\text{arr}}(\bar{x}_b)$ (Equation 32) always provides a good approximation of the arrest length by a fracture energy barrier.

4.4.3. Progressive Decay of Available Energy

As in the case of stress barriers, the one-dimensional stress intensity factor defined in Equation 28 can be readily used to predict the arrest of a crack-like rupture under smoothly decaying pre-stress conditions as $\bar{K}\left(\bar{L}_{\text{arr}}\right) = 0$. In the case of the linearly decaying shear stress $\bar{\tau}_k = 1 - \bar{\alpha}\bar{x}$, the arrest length corresponds then to $\bar{L}_{\text{arr}} = 2/\bar{\alpha}$ and is twice larger than in the case of a pulse-like rupture. For quadratic decay of the pre-stress $\bar{\tau}_k = 1 - \bar{\lambda}\bar{x}^2$, the arrest length corresponds then to $\bar{L}_{\text{arr}} = \sqrt{3/\bar{\lambda}}$. Using this arrest prediction, the one-dimensional energy balance can be used to derive a theoretical prediction of the profile of the final slip $\bar{u}_p$, as detailed in Text S4.2 in Supporting Information S1. As shown in Figure 8, the solution allows to collapse the final slip profile simulated with different values of $\bar{\alpha}$ and $\bar{\lambda}$. Important differences exist between the slip profile after pulse-like rupture shown in Figure 6 and the slip observed after crack-like rupture in Figure 8. Slip profiles after pulse-like rupture record the initial variations of the pre-stress before the rupture, whereas crack-like rupture tends to homogenize and average local variations of pre-stress. Mechanically, this difference arises because crack releases energy over the entire rupture length $\bar{L}$, whereas pulse energy balance is more local and concentrated in the thin width $\bar{\omega}$ near the rupture tip. Mathematically, this difference translates into slip profile governed by a differential equation for pulses, Equation 18, versus an integral equation that governs $\bar{u}_p$ for cracks, Equation 28. Consequently, when propagating toward decaying pre-stress, slip pulses produce asymmetric slip profiles, whereas crack-like ruptures produce slip profiles where the relative position of the maximum slip often lies between one third and one half of the

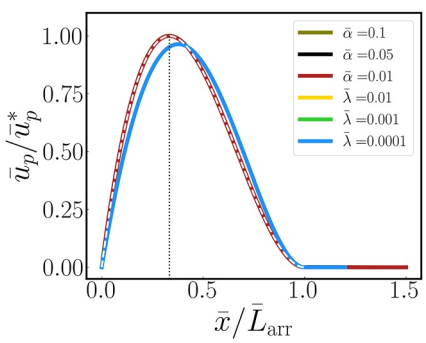

Figure 8. Simulations (solid line) versus theoretical prediction (white dashed-line) of the final slip profile observed for a crack-like rupture with a linear decay $(\bar{\tau}_k(\bar{x}) = 1 - \bar{\alpha}\bar{x})$ or a quadratic decay $\left(\bar{\tau}_k(\bar{x}) = 1 - \bar{\lambda}\bar{x}^2\right)$ of the pre-stress. As derived in Text S4.2 in Supporting Information S1, $\bar{L}_{\text{arr}}$ corresponds respectively to $2/\bar{\alpha}$ and $\sqrt{3/\bar{\lambda}}$ for the linear and quadratic decays, whereas the maximum slip $\bar{u}^*_p$ is respectively given by $4/\left(27\bar{\alpha}^2\right)$ and $2/\left(9\bar{\lambda}\right)$. The position of maximum slip is most often located near $\bar{x} = \bar{L}_{\text{arr}}/3$, as highlighted by the vertical black dotted line.

arrest distance $\bar{L}_{\text{arr}}$. Consequently, in this setup, pronounced asymmetric, triangular, slip profiles are exclusively the signature of pulse-like ruptures.

5. Discussion

5.1. Relation to Discrete Burridge-Knopoff Models

The differential equation solved in our one-dimensional model can be related to the equation of motion of spring-block systems used in Burridge-Knopoff models (Burridge & Halliday, 1971; Burridge & Knopoff, 1967). This discrete approach builds upon the standard "spring-block" analog for faulting and offers a minimal system where elasticity and friction compete in producing stick-slip and rupture cycles. Despite their simplicity, Burridge-Knoppoff models received a significant attention in the literature, notably as tools to reproduce the diversity and statistical distribution of earthquake sizes and to discuss the conditions for self-organized criticality in fault systems (Olami et al., 1992). On the other hand, the quantitative applicability of Burridge-Knopoff models to describe fault zones has often be questioned, notably because of the lack of a well-defined continuum limit as the block size is reduced (Rice, 1993). In this context, our one-dimensional system of equations brings an additional length scale H that is missing in the classical spring-block models and features well-defined continuum limits when $\Delta\bar{x} \to 0$ as shown in Figure S1 in Supporting Information S1 and detailed further in Text S2 in Supporting Information S1. In practice, H is a key length scale of the model, which appears in the scaling of most of the dimensionless variables (see Table 2) and provides physical constraints on the value of the longitudinal and leaf spring constants of Burridge-Knopoff models.

5.2. Relation to Continuum Elastic Models

The proposed one-dimensional approach also relates to continuum elastic models that have been proposed in the literature to describe faulting processes. As detailed hereafter, our one-dimensional model under imposed-stress boundary conditions provides qualitative insights into the early stage of earthquake propagation, whereas under imposed-displacement boundary conditions it provides quantitative predictions of the later stage of earthquake propagation that saturates the width of the seismogenic zone.

Under imposed-stress boundary conditions ($\Gamma = 0$), ruptures simulated with the one-dimensional model have similar dynamics to that of cracks propagating in unbounded elastic domain. In such setup, the most frequent rupture mode corresponds to the propagation of a shear crack (e.g., Ida, 1972; Kostrov, 1966), whereas slip-pulses are inherently unstable and emerge under specific loading and interface conditions (Brantut et al., 2019; Brener et al., 2018; Gabriel et al., 2012; Zheng & Rice, 1998). As in the one-dimensional model under imposed-stress boundary conditions, the system supplies an unlimited amount of energy to the propagating rupture and promotes crack-like rupture whose energy release rate increases with the rupture size. The one-dimensional setup includes an additional length scale H, such that the crack energy release rate scales as $G \sim (\Delta\tau)^2\mathcal{G}^{-1}L^2H^{-1}$ instead of the scaling $G \sim (\Delta\tau)^2\mathcal{G}^{-1}L$ relevant for circular cracks in an infinite domain. Apart from this different scaling, the crack arrest criterion predicted by Equation 28 is the one-dimensional analog of the shear fracture criterion that was successfully used to predict the arrest of frictional rupture in laboratory experiments (Bayart et al., 2016; Kammer et al., 2015; Ke et al., 2018).

Under displacement-controlled boundary conditions ($\Gamma = 1$), the rupture dynamics is substantially different and pulse-like rupture becomes the prominent failure mode. This fundamental change is caused by the finite amount of strain energy available for rupture under imposed-displacement boundary conditions. Such transition is analogous to the change in the rupture dynamics reported in three-dimensional simulations of earthquake ruptures with large aspect ratio $L \gg W$ (Day, 1982; Weng & Ampuero, 2019) or if the fault is surrounded by a damaged region with high elastic contrast (Idini & Ampuero, 2020). As depicted in Figure 1, the relevant type of boundary conditions applied at a distance H from the fault corresponds to imposed-displacement. For subduction zones (Figure 1a), the plate is loaded by and coupled to the downward motion of the viscous upper mantle. Due to the no-slip boundary conditions between the elastic plate and the viscous upper mantle, a constant displacement at the plate edge is a reasonable approximation over the duration of the dynamic ruptures. For the strike-slip system (Figure 1b), slip along the fault leads to an associated stress drop in the compliant elastic fault core of thickness H. The continuity of displacements and stress at the boundary between the compliant fault core and the stiffer wall-rock implies that the associated displacement at this boundary will be much smaller than interfacial

slip. Therefore, imposed-displacement boundary conditions is also relevant in such configurations (see Section C2 of Thøgersen et al. (2021) for more details).

Recently, Weng and Ampuero (2019) showed how the Linear Elastic Fracture Mechanics solution for a thin-strip geometry (Marder, 1998) can accurately describe earthquake dynamics at high aspect ratio L/W. Using the thin-strip solution, they proposed a *fault rupture potential* than can be used to predict the arrest and the size of earthquakes. As detailed in Text S6 in Supporting Information S1, their thin-strip solution and associated fault rupture potential are complementary to the approach proposed in the present study, which brings estimates of the final slip profile and associated stress drop and generalizes the description beyond the Linear Elastic Fracture Mechanics assumptions (finite fracture energy, small scale-yielding conditions, smooth rupture acceleration). Remarkably, the two descriptions share the same fracture energy criterion to predict rupture deceleration and lead to similar arrest length prediction in the limit $\bar{G}_c \to \bar{G}_c^*$ (see Figure S5 in Supporting Information S1).

5.3. Controls on Earthquake Arrest

Using our minimal model, we propose a pulse equation, summarized hereafter, that can describe the propagation of large planar earthquake ruptures and capture different arrest scenarios:

$$\frac{\partial^2 \bar{u}_p}{\partial \bar{x}^2} = \bar{\gamma}\bar{u}_p(\bar{x}) - \bar{\delta}(\bar{x})\bar{\tau}_k(\bar{x}). \tag{34}$$

We recall that $\bar{\tau}_k$ describes the initial stress conditions along the fault before the rupture, $\bar{u}_p$ corresponds to the total slip observed along the fault after the rupture, and $\bar{\delta}$ is a parameter defined in Equation 23 which only depends on the fracture energy and whose value lies between 1 (for the largest admissible fracture energy $\bar{G}_c = \bar{G}_c^*$) and 2 (for negligible fracture energy $\bar{G}_c = 0$). Next, we discuss how to connect the arrest of earthquakes to the different types of scenarios and arrest lengths predicted with our minimal model in Section 4.

5.3.1. Geometrical Barriers—Fault Bends

Some restraining fault bends are observed to stop ruptures whether others only slow them down (e.g., Elliott et al., 2015; King & Nábělek, 1985). One can parameterize this geometrical structure by a change in pre-stress (e.g., Lozos et al., 2011). For example, Figure 9a illustrates a restraining bend. After projection of remotely applied principle stresses on inclined planes, it is readily shown that the shear stress, τ_0, on the bend segment is reduced relative to the straight fault segments, while the normal stress σ_n on the bend is increased relative to the straight fault segment, which we assume is favorably oriented for sliding. Both these trends act to reduce the ratio $\bar{\tau}_0/\sigma_n$ in Equation 3 on the bend. Therefore, a restraining bend (Figure 9a) is a similar scenario to the stress barrier displayed in Figure 4b. Since scaling in Equation 3 assumed a constant σ_n, we note that the calculation of $\bar{\tau}_k$ must be modified to account for spatially varying $\sigma_n(x)$ and to quantify the reduction of pre-stress over the bend segment.

As sketched in Figure 9a, the amplitude of the pre-stress within the barrier ideally depends on the angle of the restraining bend θ and its length depends on the bend segment length. One can therefore use our minimal model to predict quantitatively at which angles and which lengths of bend segments the rupture will stop. Remarkably, from the generic arrest conditions $\bar{\tau}_k < 0$, our one-dimensional model predicts (see Text S5 and Figure S4 in Supporting Information S1) that $\theta = 30^\circ$ is the steepest bend angle that an earthquake rupture can traverse. Field measurements estimate this steepest bend angle at about 30° for strike-slip systems, as in Figure 1b (Barka & Kadinsky-Cade, 1988; Biasi & Wesnousky, 2017). Our pulse arrest relationship of Equation 20, and the corresponding Figure 5a, predict that the steeper the bend angle, the shorter the arrest length will be because $\bar{\tau}_{k,b}$ will decrease with increasing bend angle. Thus, we can qualitatively predict that pulses will traverse relatively long shallowly inclined bends, but will be stopped by much shorter steep bends, in agreement with Figure 4b in Lozos et al. (2011).

Note that this one-dimensional description only accounts for the possibility that rupture cross the fault bend. In natural systems, other scenarios are possible at bend segments, such as the formation of a secondary fault along a more favorable direction (Fliss, 2005). In this context, the rupture advances by breaking a fresh portion of the rock, which has a larger fracture energy as in the case of fault gaps discussed in the next paragraph.

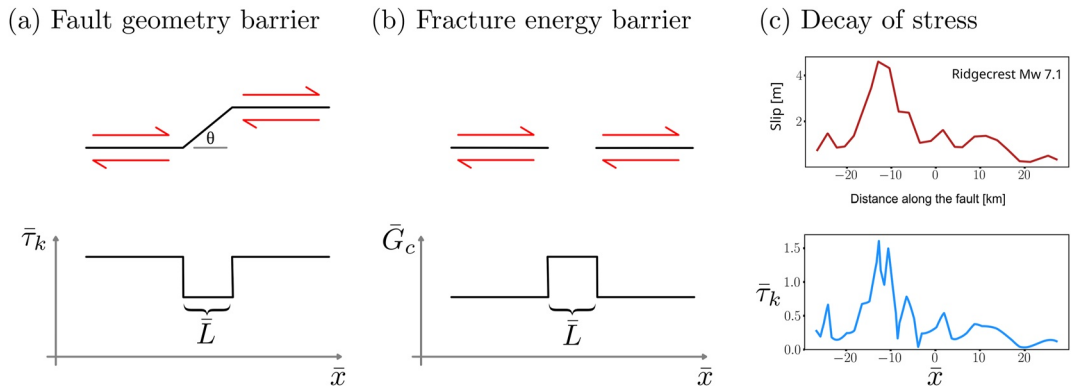

Figure 9. Cartoon of arrest scenarios and how they correspond to the different arrest scenarios discussed in Figure 3. (a) A fault bend with an angle θ and length $\bar{L}$ corresponds to a decrease in $\bar{\tau}_k$. (b) A fault gap of length $\bar{L}$ along the fault corresponds to a fracture energy barrier and is represented by a lateral increase of $\bar{G}_c$ in our model. (c) Top plot shows the profile of slip from the M_w7.1 2019 Ridgecrest earthquake published by Chen et al. (2020). The bottom plot shows the corresponding profile of dimensionless pre-stress computed using our pulse Equation 34. See more details in Text S7 in Supporting Information S1.

5.3.2. Geometrical Barrier—Fault Gaps and Step-Overs

It is known that earthquakes often stop at fault gaps, a situation depicted in Figure 9b, upper panel, which can be intact or more often made of faulted and cracked rock. Here, we follow Husseini et al. (1975) and suggest that the region of the gap can hence be described as a region with larger fracture energy, as in Figure 9b. We showed in Figure 5b that for pulses the arrest length $\bar{L}_{\text{arr}}$ increases as the material in the step-over between segments becomes weaker, that is, $\bar{G}_c$ decreases. The value of $\bar{L}_{arr}$ is shown to range between $\sim$1 and 10. If we bring this back to dimensional terms, the arrest length is in the range $H - 10H$. In the scenario described in Figure 1b, we recall that H corresponds to the thickness of the damage zone, which for mature strike-slip faults is in the range of few hundreds of meters to few kilometers (Ben-Zion & Sammis, 2003; Cocco et al., 2023; Rockwell & Ben-Zion, 2007; Savage & Brodsky, 2011).

Fault step-overs represent a geological setting combining the situations depicted in Figures 9a and 9b, where the rupture has to break a portion of intact rock and potentially to rotate. Remarkably, the arrest lengths predicted by the one-dimensional model agree with the observations that fault step-overs exceeding five km across the fault mostly stop earthquakes (Barka & Kadinsky-Cade, 1988; Biasi & Wesnousky, 2021). Moreover, the scaling behind our model predicts that the thicker the damage zone, the larger the step-over that earthquakes can traverse, which is consistent with field evidence for large step-over widths along more mature fault zones (Manighetti et al., 2021).

5.3.3. Variable Stress Conditions

In the Earth's crust, the pre-stress along a fault varies continuously due to tectonic loading, spatially and temporally varying slip, and earthquake-induced Coulomb stress transfer to and from neighboring faults among other processes such as fluid motions. These processes increase or decrease pre-stress magnitude and heterogeneity with time. For example, Mildon et al. (2019) showed that the magnitude of pre-stress heterogeneity on faults in the Apennines exceeds 5 MPa, due to cumulative addition of Coulomb stress transfer of known earthquakes from the last 660 years, and an additional strong pre-stress heterogeneous component arising from irregular fault geometry, in particular from bends on faults, as discussed in Section 5.3.1 above. Examples of pre-stress variations unrelated to fault geometry include the 1966 Parkfield earthquake arrest, attributed to a seismic velocity anomaly in the lower crust (Aki, 1979), and pore pressure injections that may extend induced earthquake size (Galis et al., 2017). On top of the initial variability in pre-stress, each subsequent rupture event further evolves the pre-stress (Duan & Oglesby, 2005).

Remarkably, the pulse Equation 34 proposed in the present study illuminates the stress distribution along the fault before and after the earthquake. As a proof of concept, we demonstrate how the pulse Equation 34 can be applied to seismic data. To this aim, we select the M_w7.1 Ridgecrest earthquake in 2019, whose late-stage rupture dynamics becomes similar to the one-dimensional planar pulse described by our model (see Figure 2 of

Chen et al. (2020)). The slip profile after the event u_p is assumed from the surface slip measurement computed by Chen et al. (2020) using optical correlation of satellite images (recalled in the top panel of Figure 9c). Using the physical parameters and procedure summarized in Supporting Information S1 (see Text S7 and Figure S6 in Supporting Information S1), the slip profile is first transformed into the dimensionless variables $\bar{u}_p$ and then plugged into the pulse Equation 34 to obtain an estimate of the profile of $\bar{\tau}_k$ before the rupture (shown in the bottom panel of Figure 9c).

5.4. Planar-Pulse Versus Circular-Crack Models

The one-dimensional pulse rupture discussed in the present study has some important differences with the dynamics of circularly growing crack, each of them representing two end-member situations of the earthquake cycle. Such a transition from crack to pulse once the crack saturates the seismogenic layer, is observed to occur in large strike-slip earthquakes, for example, the 2019 M_w7.1 Ridgecrest earthquake (Chen et al., 2020), and the 2021 M_w7.4 Madoi earthquake (Chen et al., 2022). Apart from stable pulse-like solution discussed previously, planar rupture produces some interesting features of earthquake dynamics that remains debated in the circular-crack framework and could be explored in prospective works, notably the connection between the stress drop and the initial pre-stress along the fault.

Using the pulse Equation 34, the state of stress after the rupture can be predicted from the slip profile $\bar{u}_p$. As detailed in Equations S63 and S64 in Supporting Information S1, the stress drop in the one-dimensional model is given by $\bar{\delta}\bar{\tau}_k$ or, in dimensional units,

$$\Delta\tau = \bar{\delta}(\tau_0 - \mu_k\sigma_n), \tag{35}$$

Unlike circular crack model, planar pulse-like ruptures have then a stress drop independent of the rupture radius/size and linearly dependent on the initial state of shear stress τ_0 acting on the fault before the event. Interestingly, this property of one-dimensional planar rupture implies that the final slip profile measured along fault zones after an earthquake could provide information both on the initial shear stress before the rupture (as described in Figure 9c) but also after the rupture by subtracting the stress drop predicted in Equation 35.

5.4.1. Back-Propagating Fronts at the Arrest Location

During the rupture arrests simulated in this paper, back-propagating fronts are sometimes observed after the sharp arrest of the main pulse front (e.g., by a stress or fracture energy barriers). As displayed in Figure S7 in Supporting Information S1, such fronts correspond to pulses of negative slip velocity that nucleate at the arrest location and propagate back to the nucleation zone. Back-propagating fronts are direct consequences of the stress drop described in Equation 35 and the fact that one-dimensional planar rupture can reverse the sign of the shear stress along the interface. If the resulting negative shear stress is below the kinetic friction for negative slip (i.e., $\tau_0 - \Delta\tau < -\mu_k\sigma_n$), the interface is critically loaded and can host back-propagating fronts. Text S8 and Figure S7 in Supporting Information S1 discuss how these secondary ruptures can be described by the same pulse theory presented in this paper and arise if the initial shear stress satisfies the following criterion:

$$\tau_0 > \frac{\bar{\delta}+1}{\bar{\delta}-1}\mu_k\sigma_n \geq 3\mu_k\sigma_n. \tag{36}$$

Recently, Idini and Ampuero (2020) reported traveling back-propagating fronts in numerical simulations of earthquake cycles within a low-velocity fault zone and discuss how recent progress in seismic monitoring allowed to detect secondary rupture fronts propagating with a reverse slip direction compared to the main rupture event. The presence of this low-velocity fault core (as shown in Figure 1) and the pulse-like nature of these back-propagating fronts suggest some direct analogies with the response of our one-dimensional model.

5.4.2. Triangular Slip Profile

Slip profiles of faults and earthquakes often display a triangular shape (Manighetti et al., 2001, 2004, 2005; Scholz, 2019). These profiles have been observed to have a characteristic asymmetry, where the short edge of

the triangle is often closer to the hypocenter of the earthquake, the position of the maximum slip position is not constant and varies among earthquakes (Manighetti et al., 2005). So far only a few models have been proposed to explain this observation. Manighetti et al. (2004) suggested that off-fault damage and plasticity account for the triangular slip distribution. Because faults grow laterally over time, there is a lateral gradient in maturity and hence damage compliance. Cappa et al. (2014) suggested that the moduli of the off-fault damaged zone varies along the fault. They demonstrated that this variation produces a triangular profile. In fact, this variation of moduli will produce a variation in available strain energy stored along the fault, and therefore this is equivalent to the slip pulse evolution when there is a depletion of strain energy scenario, that we describe in Figures 3d and 6. Thus, $\bar{\tau}_k$ in our model encapsulates the backbone physics of the scenario of Cappa et al. (2014) and Manighetti et al. (2004), yet offers a larger set of scenarios for obtaining triangular slip: any slip pulse that propagates into regions of decreasing pre-stress or elastic strain energy will produce such a profile. In fact, our work suggests that triangular slip profiles may be a signature of pulse-like earthquakes that have been stopped by a depletion in available strain energy, which translates into depletion in $\bar{\tau}_k$.

6. Conclusion

To study frictional rupture arrest, we present a one-dimensional model that brings a characteristic length scale H to the standard Burridge-Knopoff model and bridges it to continuum fault models. The model captures the two types of boundary conditions relevant at the early and late stage of earthquake rupture and reveals their fundamental impact on the style of the rupture (crack vs. pulse), its energy balance, and the arrest conditions. Under imposed-displacement boundary conditions, the proposed one-dimensional model provides a good approximation for the dynamics of large earthquake ruptures that saturate the width of the seismogenic zone and propagate as planar front (as sketched in Figure 1). In this context, the main conclusions are:

- The formulation of the model is minimal and generic and allows to wrap various earthquake arrest scenarios into the variations of two dimensionless variables $\bar{\tau}_k$ (dimensionless stress parameter that describes the initial state of stress along the fault) and $\bar{G}_c$ (dimensionless fracture energy that characterizes the amount of breakdown work required to weaken fault friction down to the residual stress).
- Using these two parameters, we propose simple scaling relationships to characterize the arrest length of earthquakes.
- The stress drop depends linearly on the initial pre-stress.
- The regions of the fault that will arrest the next large earthquake can be predicted independently of where the rupture will nucleate.
- The transition from circular crack growth to the propagation of planar pulse brings new insight on unsettled features of natural earthquakes such as the observed asymmetric, triangular, slip profile along fault zones, the conditions for back-propagating ruptures, and the prevalence of the pulse-like rupture style for large earthquakes.

The proposed one-dimensional formulation is generic and can be the backbone of different kinds of future developments and studies. This paper aims at providing a minimal description of frictional systems but can readily account for more sophisticated models including rate-dependent friction laws. Future studies can investigate if rupture arrested by a local change in rate-dependent properties (e.g., velocity strengthening barrier) can be mapped and predicted as a combined change in dimensionless fracture energy $\bar{G}_c$ and stress parameter $\bar{\tau}_k$.

As shown in Figure 1b, the one-dimensional model under imposed-displacement boundary conditions can describe the response of a low velocity fault zone that is much more compliant than the surrounding wall rock. In natural systems, the damage, plasticity and compliance of the low velocity fault zone are expected to evolve both spatially along the fault according to the gradient in fault maturity (Cappa et al., 2014), but also temporally as a dynamic result of the rupture (Ben-Zion & Dresen, 2022; Mia et al., 2022). The proposed model can be extended to account for finite contrast of compliance between the damage zone and the wall rock, for instance by including a viscous term $\bar{v}\dot{\bar{u}}$ on the right hand side of Equation 1 to account for radiation damping effects, that is, mechanical energy lost as elastic waves in the surrounding bulk (Barras et al., 2019).

The simulations shown in Figure 3 highlight the propensity of pulse-like ruptures to produce frictional slip that mimics the initial profile of stress, which has also been reported in two-dimensional antiplane simulations (Chapter 5.7 of Elbanna (2011)). The interaction of pulse-like rupture with heterogeneous pre-stress over different length scales can be investigated by future works in light of the pulse Equation 34 proposed in this paper.

In the context of earthquakes and faulting, imposed-displacement is the most relevant type of boundary conditions. Nevertheless, the proposed dimensionless formulation is generic and can be extended to a broad kind of rheologies and geological systems, including geohazards driven by gravity for which imposed-stress configurations is relevant, such as landslides (Germanovich et al., 2016) or snow slab avalanches (Trottet et al., 2022).

Data Availability Statement

The code and scripts used to run the simulations, analyze data and produce the figures of this publication and Supporting Information have been archived and are freely accessible on Zenodo: https://zenodo.org/record/7788014.

Acknowledgments
This project has received funding from the Research Council of Norway (project "History Dependent Friction," Grant 287084) and the European Research Council (ERC) under the European Union's Horizon 2020 research and innovation program (Grant agreement No. 101019628 BREAK). The authors thank Yehuda Ben-Zion for insightful discussion during this work. The authors are also thankful to Editor Isabelle Manighetti, an anonymous Associate Editor, the reviewers Huihui Weng and Ahmed Elbanna for thorough reviews and valuable comments on the manuscript.

References

Abercrombie, R. E., & Rice, J. R. (2005). Can observations of earthquake scaling constrain slip weakening? *Geophysical Journal International*, *162*(2), 406–424. https://doi.org/10.1111/j.1365-246x.2005.02579.x

Agliardi, F., Scuderi, M. M., Fusi, N., & Collettini, C. (2020). Slow-to-fast transition of giant creeping rockslides modulated by undrained loading in basal shear zones. *Nature Communications*, *11*(1), 1–11. https://doi.org/10.1038/s41467-020-15093-3

Aki, K. (1979). Characterization of barriers on an earthquake fault. *Journal of Geophysical Research*, *84*(B11), 6140–6148. https://doi.org/10.1029/jb084ib11p06140

Amundsen, D. S., Scheibert, J., Thøgersen, K., Trømborg, J., & Malthe-Sørenssen, A. (2012). 1D model of precursors to frictional stick-slip motion allowing for robust comparison with experiments. *Tribology Letters*, *45*(2), 357–369. https://doi.org/10.1007/s11249-011-9894-3

Barka, A., & Kadinsky-Cade, K. (1988). Strike-slip fault geometry in Turkey and its influence on earthquake activity. *Tectonics*, *7*(3), 663–684. https://doi.org/10.1029/tc007i003p00663

Barras, F., Aldam, M., Roch, T., Brener, E. A., Bouchbinder, E., & Molinari, J.-F. (2019). Emergence of cracklike behavior of frictional rupture: The origin of stress drops. *Physical Review X*, *9*(4), 041043. https://doi.org/10.1103/PhysRevX.9.041043

Barras, F., Aldam, M., Roch, T., Brener, E. A., Bouchbinder, E., & Molinari, J.-F. (2020). The emergence of crack-like behavior of frictional rupture: Edge singularity and energy balance. *Earth and Planetary Science Letters*, *531*, 115978. https://doi.org/10.1016/j.epsl.2019.115978

Bayart, E., Svetlizky, I., & Fineberg, J. (2016). Fracture mechanics determine the lengths of interface ruptures that mediate frictional motion. *Nature Physics*, *12*(2), 166–170. https://doi.org/10.1038/nphys3539

Ben-Zion, Y., & Dresen, G. (2022). A synthesis of fracture, friction and damage processes in earthquake rupture zones. *Pure and Applied Geophysics*, *179*(12), 4323–4339. https://doi.org/10.1007/s00024-022-03168-9

Ben-Zion, Y., & Sammis, C. G. (2003). Characterization of fault zones. *Pure and Applied Geophysics*, *160*(3), 677–715. https://doi.org/10.1007/pl00012554

Biasi, G. P., & Wesnousky, S. G. (2017). Bends and ends of surface ruptures. *Bulletin of the Seismological Society of America*, *107*(6), 2543–2560. https://doi.org/10.1785/0120160292

Biasi, G. P., & Wesnousky, S. G. (2021). Rupture passing probabilities at fault bends and steps, with application to rupture length probabilities for earthquake early warning. *Bulletin of the Seismological Society of America*, *111*(4), 2235–2247. https://doi.org/10.1785/0120200370

Brantut, N., Garagash, D. I., & Noda, H. (2019). Stability of pulse-like earthquake ruptures. *Journal of Geophysical Research: Solid Earth*, *124*(8), 8998–9020. https://doi.org/10.1029/2019JB017926

Braun, O. M., Barel, I., & Urbakh, M. (2009). Dynamics of transition from static to kinetic friction. *Physical Review Letters*, *103*(19), 194301. https://doi.org/10.1103/PhysRevLett.103.194301

Brener, E. A., Aldam, M., Barras, F., Molinari, J.-F., & Bouchbinder, E. (2018). Unstable slip pulses and earthquake nucleation as a nonequilibrium first-order phase transition. *Physical Review Letters*, *121*(23), 234302. https://doi.org/10.1103/PhysRevLett.121.234302

Brener, E. A., & Bouchbinder, E. (2021). Unconventional singularities and energy balance in frictional rupture. *Nature Communications*, *12*(1), 2585. https://doi.org/10.1038/s41467-021-22806-9

Brown, S. R., Scholz, C. H., & Rundle, J. B. (1991). A simplified spring-block model of earthquakes. *Geophysical Research Letters*, *18*(2), 215–218. https://doi.org/10.1029/91GL00210

Burridge, R., & Halliday, G. (1971). Dynamic shear cracks with friction as models for shallow focus earthquakes. *Geophysical Journal International*, *25*(1–3), 261–283. https://doi.org/10.1111/j.1365-246x.1971.tb02339.x

Burridge, R., & Knopoff, L. (1967). Model and theoretical seismicity. *Bulletin of the Seismological Society of America*, *57*(3), 341–371. https://doi.org/10.1785/BSSA0570030341

Cappa, F., Perrin, C., Manighetti, I., & Delor, E. (2014). Off-fault long-term damage: A condition to account for generic, triangular earthquake slip profiles. *Geochemistry, Geophysics, Geosystems*, *15*(4), 1476–1493. https://doi.org/10.1002/2013gc005182

Carlson, J. M., Langer, J. S., & Shaw, B. E. (1994). Dynamics of earthquake faults. *Reviews of Modern Physics*, *66*(2), 657–670. https://doi.org/10.1103/RevModPhys.66.657

Chen, K., Avouac, J.-P., Aati, S., Milliner, C., Zheng, F., & Shi, C. (2020). Cascading and pulse-like ruptures during the 2019 Ridgecrest earthquakes in the Eastern California Shear Zone. *Nature Communications*, *11*(1), 22. https://doi.org/10.1038/s41467-019-13750-w

Chen, K., Avouac, J.-P., Geng, J., Liang, C., Zhang, Z., Li, Z., & Zhang, S. (2022). The 2021 M_w 7.4 Madoi earthquake: An archetype bilateral slip-pulse rupture arrested at a splay fault. *Geophysical Research Letters*, *49*(2), e2021GL095243. https://doi.org/10.1029/2021GL095243

Cocco, M., Aretusini, S., Cornelio, C., Nielsen, S. B., Spagnuolo, E., Tinti, E., & Di Toro, G. (2023). Fracture energy and breakdown work during earthquakes. *Annual Review of Earth and Planetary Sciences*, *51*(1), 217–252. https://doi.org/10.1146/annurev-earth-071822-100304

Cromer, A. (1981). Stable solutions using the Euler approximation. *American Journal of Physics*, *49*(5), 455–459. https://doi.org/10.1119/1.12478

Das, S., & Aki, K. (1977). Fault plane with barriers: A versatile earthquake model. *Journal of Geophysical Research*, *82*(36), 5658–5670. https://doi.org/10.1029/jb082i036p05658

Day, S. M. (1982). Three-dimensional finite difference simulation of fault dynamics: Rectangular faults with fixed rupture velocity. *Bulletin of the Seismological Society of America*, *72*(3), 705–727. https://doi.org/10.1785/BSSA0720030705

Duan, B., & Oglesby, D. D. (2005). Multicycle dynamics of nonplanar strike-slip faults. *Journal of Geophysical Research*, *110*(B3), B03304. https://doi.org/10.1029/2004jb003298

Elbanna, A. E. (2011). Pulselike ruptures on strong velocity-weakening frictional interfaces: Dynamics and implications (Doctoral dissertation). California Institute of Technology. https://doi.org/10.7907/80MV-6Y66
Elbanna, A. E., & Heaton, T. H. (2012). A new paradigm for simulating pulse-like ruptures: The pulse energy equation. *Geophysical Journal International*, *189*(3), 1797–1806. https://doi.org/10.1111/j.1365-246x.2012.05464.x
Elliott, A. J., Oskin, M. E., Liu-Zeng, J., & Shao, Y. (2015). Rupture termination at restraining bends: The last great earthquake on the Altyn Tagh fault. *Geophysical Research Letters*, *42*(7), 2164–2170. https://doi.org/10.1002/2015gl063107
Fliss, S. (2005). Fault branching and rupture directivity. *Journal of Geophysical Research*, *110*(B6), B06312. https://doi.org/10.1029/2004JB003368
Freund, L. B. (1998). *Dynamic fracture mechanics*. Cambridge University Press.
Gabriel, A.-A., Ampuero, J.-P., Dalguer, L. A., & Mai, P. M. (2012). The transition of dynamic rupture styles in elastic media under velocity-weakening friction. *Journal of Geophysical Research*, *117*(B9), B09311. https://doi.org/10.1029/2012jb009468
Galis, M., Ampuero, J. P., Mai, P. M., & Cappa, F. (2017). Induced seismicity provides insight into why earthquake ruptures stop. *Science Advances*, *3*(12), eaap7528. https://doi.org/10.1126/sciadv.aap7528
Germanovich, L. N., Kim, S., & Puzrin, A. M. (2016). Dynamic growth of slip surfaces in catastrophic landslides. *Proceedings of the Royal Society A: Mathematical, Physical and Engineering Sciences*, *472*(2185), 20150758. https://doi.org/10.1098/rspa.2015.0758
Gvirtzman, S., & Fineberg, J. (2021). Nucleation fronts ignite the interface rupture that initiates frictional motion. *Nature Physics*, *17*(9), 1037–1042. https://doi.org/10.1038/s41567-021-01299-9
Harris, R. A., & Day, S. M. (1999). Dynamic 3D simulations of earthquakes on en echelon faults. *Geophysical Research Letters*, *26*(14), 2089–2092. https://doi.org/10.1029/1999gl900377
Heaton, T. H. (1990). Evidence for and implications of self-healing pulses of slip in earthquake rupture. *Physics of the Earth and Planetary Interiors*, *64*(1), 1–20. https://doi.org/10.1016/0031-9201(90)90002-F
Husseini, M. I., Jovanovich, D. B., Randall, M., & Freund, L. (1975). The fracture energy of earthquakes. *Geophysical Journal International*, *43*(2), 367–385. https://doi.org/10.1111/j.1365-246x.1975.tb00640.x
Ida, Y. (1972). Cohesive force across the tip of a longitudinal-shear crack and Griffith's specific surface energy. *Journal of Geophysical Research*, *77*(20), 3796–3805. https://doi.org/10.1029/JB077i020p03796
Idini, B., & Ampuero, J.-P. (2020). Fault-zone damage promotes pulse-like rupture and back-propagating fronts via quasi-static effects. *Geophysical Research Letters*, *47*(23), e2020GL090736. https://doi.org/10.1029/2020GL090736
Kammer, D. S., Radiguet, M., Ampuero, J.-P., & Molinari, J.-F. (2015). Linear elastic fracture mechanics predicts the propagation distance of frictional slip. *Tribology Letters*, *57*(3), 23. https://doi.org/10.1007/s11249-014-0451-8
Ke, C.-Y., McLaskey, G. C., & Kammer, D. S. (2018). Rupture termination in laboratory-generated earthquakes. *Geophysical Research Letters*, *45*(23), 12784–12792. https://doi.org/10.1029/2018GL080492
Ke, C.-Y., McLaskey, G. C., & Kammer, D. S. (2022). Earthquake breakdown energy scaling despite constant fracture energy. *Nature Communications*, *13*(1), 1005. https://doi.org/10.1038/s41467-022-28647-4
King, G., & Nábělek, J. (1985). Role of fault bends in the initiation and termination of earthquake rupture. *Science*, *228*(4702), 984–987. https://doi.org/10.1126/science.228.4702.984
Knopoff, L., & Ni, X. X. (2001). Numerical instability at the edge of a dynamic fracture. *Geophysical Journal International*, *147*(3), 1–6. https://doi.org/10.1046/j.1365-246x.2001.01567.x
Kostrov, B. (1966). Unsteady propagation of longitudinal shear cracks. *Journal of Applied Mathematics and Mechanics*, *30*(6), 1241–1248. https://doi.org/10.1016/0021-8928(66)90087-6
Kostrov, B., & Das, S. (1988). *Principles of earthquake source mechanics*. Cambridge University Press.
Lambert, V., & Lapusta, N. (2020). Rupture-dependent breakdown energy in fault models with thermo-hydro-mechanical processes. *Solid Earth*, *11*(6), 2283–2302. https://doi.org/10.5194/se-11-2283-2020
Lambert, V., Lapusta, N., & Perry, S. (2021). Propagation of large earthquakes as self-healing pulses or mild cracks. *Nature*, *591*(7849), 252–258. https://doi.org/10.1038/s41586-021-03248-1
Lozos, J. C., Oglesby, D. D., Duan, B., & Wesnousky, S. G. (2011). The effects of double fault bends on rupture propagation: A geometrical parameter study. *Bulletin of the Seismological Society of America*, *101*(1), 385–398. https://doi.org/10.1785/0120100029
Madariaga, R. (1976). Dynamics of an expanding circular fault. *Bulletin of the Seismological Society of America*, *66*(3), 639–666. https://doi.org/10.1785/bssa0660030639
Manighetti, I., Campillo, M., Sammis, C., Mai, P. M., & King, G. (2005). Evidence for self-similar, triangular slip distributions on earthquakes: Implications for earthquake and fault mechanics. *Journal of Geophysical Research*, *110*(B5), B05302. https://doi.org/10.1029/2004jb003174
Manighetti, I., King, G., Gaudemer, Y., Scholz, C., & Doubre, C. (2001). Slip accumulation and lateral propagation of active normal faults in Afar. *Journal of Geophysical Research*, *106*(B7), 13667–13696. https://doi.org/10.1029/2000jb900471
Manighetti, I., King, G., & Sammis, C. G. (2004). The role of off-fault damage in the evolution of normal faults. *Earth and Planetary Science Letters*, *217*(3–4), 399–408. https://doi.org/10.1016/s0012-821x(03)00601-0
Manighetti, I., Mercier, A., & De Barros, L. (2021). Fault trace corrugation and segmentation as a measure of fault structural maturity. *Geophysical Research Letters*, *48*(20), e2021GL095372. https://doi.org/10.1029/2021GL095372
Marder, M. (1998). Adiabatic equation for cracks. *Philosophical Magazine B*, *78*(2), 203–214. https://doi.org/10.1080/13642819808202942
Marone, C., & Scholz, C. (1988). The depth of seismic faulting and the upper transition from stable to unstable slip regimes. *Geophysical Research Letters*, *15*(6), 621–624. https://doi.org/10.1029/gl015i006p00621
Mia, M. S., Abdelmeguid, M., & Elbanna, A. E. (2022). Spatio-temporal clustering of seismicity enabled by off-fault plasticity. *Geophysical Research Letters*, *49*(8), e2021GL097601. https://doi.org/10.1029/2021GL097601
Middleton, T. A., Walker, R. T., Parsons, B., Lei, Q., Zhou, Y., & Ren, Z. (2016). A major, intraplate, normal-faulting earthquake: The 1739 Yinchuan event in northern China: 1739 Yinchuan Earthquake, Northern China. *Journal of Geophysical Research: Solid Earth*, *121*(1), 293–320. https://doi.org/10.1002/2015JB012355
Mildon, Z., Roberts, G. P., Walker, J. F., & Toda, S. (2019). Coulomb pre-stress and fault bends are ignored yet vital factors for earthquake triggering and hazard. *Nature Communications*, *10*(1), 1–9. https://doi.org/10.1038/s41467-019-10520-6
Olami, Z., Feder, H. J. S., & Christensen, K. (1992). Self-organized criticality in a continuous, nonconservative cellular automaton modeling earthquakes. *Physical Review Letters*, *68*(8), 1244–1247. https://doi.org/10.1103/PhysRevLett.68.1244
Paglialunga, F., Passelègue, F., Brantut, N., Barras, F., Lebihain, M., & Violay, M. (2021). On the scale dependence in the dynamics of frictional rupture: Constant fracture energy versus size-dependent breakdown work. *Earth and Planetary Science Letters*, *584*, 117442. https://doi.org/10.1016/j.epsl.2022.117442
Palmer, A. C., & Rice, J. R. (1973). The growth of slip surfaces in the progressive failure of over-consolidated clay. *Proceedings of the Royal Society of London. A. Mathematical and Physical Sciences*, *332*(1591), 527–548. https://doi.org/10.1098/rspa.1973.0040

Perrin, C., Manighetti, I., Ampuero, J.-P., Cappa, F., & Gaudemer, Y. (2016). Location of largest earthquake slip and fast rupture controlled by along-strike change in fault structural maturity due to fault growth. *Journal of Geophysical Research: Solid Earth*, *121*(5), 3666–3685. https://doi.org/10.1002/2015jb012671

Rice, J. R. (1993). Spatio-temporal complexity of slip on a fault. *Journal of Geophysical Research*, *98*(B6), 9885. https://doi.org/10.1029/93JB00191

Roch, T., Brener, E. A., Molinari, J.-F., & Bouchbinder, E. (2022). Velocity-driven frictional sliding: Coarsening and steady-state pulses. *Journal of the Mechanics and Physics of Solids*, *158*, 104607. https://doi.org/10.1016/j.jmps.2021.104607

Rockwell, T. K., & Ben-Zion, Y. (2007). High localization of primary slip zones in large earthquakes from paleoseismic trenches: Observations and implications for earthquake physics. *Journal of Geophysical Research*, *112*(B10), B10304. https://doi.org/10.1029/2006jb004764

Savage, H. M., & Brodsky, E. E. (2011). Collateral damage: Evolution with displacement of fracture distribution and secondary fault strands in fault damage zones. *Journal of Geophysical Research*, *116*(B3), B03405. https://doi.org/10.1029/2010JB007665

Scholz, C. H. (1998). Earthquakes and friction laws. *Nature*, *391*(6662), 37–42. https://doi.org/10.1038/34097

Scholz, C. H. (2019). *The mechanics of earthquakes and faulting* (3rd ed.). Cambridge University Press. https://doi.org/10.1017/9781316681473

Sibson, R. H. (1985). Stopping of earthquake ruptures at dilational fault jogs. *Nature*, *316*(6025), 248–251. https://doi.org/10.1038/316248a0

Sibson, R. H., & Das, S. (1986). Rupture interaction with fault jogs. *Earthquake Source Mechanics*, *37*, 157–167. https://doi.org/10.1029/GM037p0157

Stein, R. S., Barka, A. A., & Dieterich, J. H. (1997). Progressive failure on the North Anatolian fault since 1939 by earthquake stress triggering. *Geophysical Journal International*, *128*(3), 594–604. https://doi.org/10.1111/j.1365-246X.1997.tb05321.x

Thøgersen, K., Aharonov, E., Barras, F., & Renard, F. (2021). Minimal model for the onset of slip pulses in frictional rupture. *Physical Review E*, *103*(5), 052802. https://doi.org/10.1103/PhysRevE.103.052802

Thøgersen, K., Gilbert, A., Schuler, T. V., & Malthe-Sørenssen, A. (2019). Rate-and-state friction explains glacier surge propagation. *Nature Communications*, *10*(1), 2823. https://doi.org/10.1038/s41467-019-10506-4

Thøgersen, K., Sveinsson, H., Scheibert, J., Renard, F., & Malthe-Sørenssen, A. (2019). The moment duration scaling relation for slow rupture arises from transient rupture speeds. *Geophysical Research Letters*, *46*(22), 12805–12814. https://doi.org/10.1029/2019gl084436

Tinti, E., Spudich, P., & Cocco, M. (2005). Earthquake fracture energy inferred from kinematic rupture models on extended faults. *Journal of Geophysical Research*, *110*(B12), B12303. https://doi.org/10.1029/2005JB003644

Trømborg, J., Scheibert, J., Amundsen, D. S., Thøgersen, K., & Malthe-Sørenssen, A. (2011). Transition from static to kinetic friction: Insights from a 2D model. *Physical Review Letters*, *107*(7), 074301. https://doi.org/10.1103/PhysRevLett.107.074301

Trømborg, J., Sveinsson, H., Scheibert, J., Thøgersen, K., Amundsen, D. S., & Malthe-Sørenssen, A. (2014). Slow slip and the transition from fast to slow fronts in the rupture of frictional interfaces. *Proceedings of the National Academy of Sciences*, *111*(24), 8764–8769. https://doi.org/10.1073/pnas.1321752111

Trottet, B., Simenhois, R., Bobillier, G., Bergfeld, B., van Herwijnen, A., Jiang, C., & Gaume, J. (2022). Transition from sub-Rayleigh anticrack to supershear crack propagation in snow avalanches. *Nature Physics*, *18*(9), 1094–1098. https://doi.org/10.1038/s41567-022-01662-4

Viesca, R. C., & Rice, J. R. (2012). Nucleation of slip-weakening rupture instability in landslides by localized increase of pore pressure. *Journal of Geophysical Research*, *117*(B3), B03104. https://doi.org/10.1029/2011JB008866

Weng, H., & Ampuero, J.-P. (2019). The dynamics of elongated Earthquake ruptures. *Journal of Geophysical Research: Solid Earth*, *124*(8), 8584–8610. https://doi.org/10.1029/2019JB017684

Wesnousky, S. G. (1988). Seismological and structural evolution of strike-slip faults. *Nature*, *335*(6188), 340–343. https://doi.org/10.1038/335340a0

Zheng, G., & Rice, J. R. (1998). Conditions under which velocity-weakening friction allows a self-healing versus a cracklike mode of rupture. *Bulletin of the Seismological Society of America*, *88*(6), 1466–1483. https://doi.org/10.1785/BSSA0880061466

References From the Supporting Information

Amundsen, D. S., Trømborg, J. K., Thøgersen, K., Katzav, E., Malthe-Sørenssen, A., & Scheibert, J. (2015). Steady-state propagation speed of rupture fronts along one-dimensional frictional interfaces. *Physical Review E*, *92*(3), 032406. https://doi.org/10.1103/physreve.92.032406

Anderson, T. L. (2005). *Fracture mechanics: Fundamentals and applications* (3rd ed.). Taylor & Francis.

Bar-Sinai, Y., Spatschek, R., Brener, E. A., & Bouchbinder, E. (2013). Instabilities at frictional interfaces: Creep patches, nucleation, and rupture fronts. *Physical Review E*, *88*(6), 060403. https://doi.org/10.1103/PhysRevE.88.060403

Bouchbinder, E., Brener, E. A., Barel, I., & Urbakh, M. (2011). Slow cracklike dynamics at the onset of frictional sliding. *Physical Review Letters*, *107*(23), 235501. https://doi.org/10.1103/PhysRevLett.107.235501

Byerlee, J. (1978). Friction of rocks. *Pure and Applied Geophysics PAGEOPH*, *116*(4–5), 615–626. https://doi.org/10.1007/BF00876528

Courant, R., Friedrichs, K., & Lewy, H. (1928). Über die partiellen Differenzengleichungen der mathematischen Physik. *Mathematische Annalen*, *100*(1), 32–74. https://doi.org/10.1007/bf01448839

Knopoff, L., Mouton, J. O., & Burridge, R. (2009). The dynamics of a one-dimensional fault in the presence of friction†. *Geophysical Journal of the Royal Astronomical Society*, *35*(1–3), 169–184. https://doi.org/10.1111/j.1365-246X.1973.tb02420.x

Muratov, C. B. (1999). Traveling wave solutions in the Burridge-Knopoff model. *Physical Review E*, *59*(4), 3847–3857. https://doi.org/10.1103/PhysRevE.59.3847